Double-distribution-function discrete Boltzmann model for combustion

Chuandong Lin[a], Aiguo Xu[b,c,d,1], Guangcai Zhang[b,d,e], Yingjun Li[a,2]

[a]*State Key Laboratory for GeoMechanics and Deep Underground Engineering, China University of Mining and Technology, Beijing 100083, P.R.China*
[b]*National Key Laboratory of Computational Physics, Institute of Applied Physics and Computational Mathematics, P. O. Box 8009-26, Beijing 100088, P.R.China*
[c]*Center for Applied Physics and Technology, MOE Key Center for High Energy Density Physics Simulations, College of Engineering, Peking University, Beijing 100871, P.R.China*
[d]*State Key Laboratory of Theoretical Physics, Institute of Theoretical Physics, Chinese Academy of Sciences,Beijing 100190, P.R.China*
[e]*State Key Laboratory of Explosion Science and Technology, Beijing Institute of Technology, Beijing 100081, P.R.China*

Abstract

A 2-dimensional discrete Boltzmann model for combustion is presented. Mathematically, the model is composed of two coupled discrete Boltzmann equations for two species and a phenomenological equation for chemical reaction process. Physically, the model is equivalent to a reactive Navier-Stokes model supplemented by a coarse-grained model for the thermodynamic nonequilibrium behaviours. This model adopts 16 discrete velocities. It works for both subsonic and supersonic combustion phenomena with flexible specific heat ratio. To discuss the physical accuracy of the coarse-grained model for nonequilibrium behaviours, three other discrete velocity models are used for comparisons. Numerical results are compared with analytical solutions based on both the first-order and second-order truncations of the distribution function. It is confirmed that the physical accuracy increases with the increasing moment relations needed by nonequlibrium manifestations. Furthermore, compared with the single distribution function model, this model can simulate more details of combustion.

[1]Corresponding author. Email addresses: Xu_Aiguo@iapcm.ac.cn
[2]Corresponding author. Email addresses: lyj@aphy.iphy.ac.cn

Keywords: Discrete Boltzmann model, Combustion, Detonation, Nonequilibrium effects
PACS: 47.11.-j, 47.40.Rs, 47.70.-n

1. Introduction

As the first controlled chemical reaction discovered by humans, combustion continues to play a dominant role in providing energy for humanity. Up to now, more than 80% of the world's energy is generated from the combustion of solids, liquids, and gases [1, 2]. Owing to the societal concern for energy sufficiency and environmental quality, the combustion research is extensively performed [3, 4, 5, 6, 7] in theoretical, experimental and numerical areas. Currently, combustion has become a quantitative and predictive scientific discipline. However, many fundamental problems have not yet been resolved, especially those related to various nonequilibrium behaviours [8, 9].

Generally, the traditional simulation of combustion is based on a hydrodynamic model combined with a phenomenological one of the chemical reaction process. The hydrodynamic model is generally a set of Euler or Navier-Stokes (NS) equations. As is known, the Euler or NS model is capable of capturing the main characteristics of hydrodynamic nonequilibrium (HNE) effects, but encounters many difficulties in describing thermodynamic nonequilibrium (TNE) effects. In the past two decades the lattice Boltzmann (LB) method has been developed as a powerful computational method for simulating multiphase flows [10, 11, 12, 13, 14, 15, 16, 17, 18], combustion phenomena [19, 20, 21, 22, 23, 24, 25, 26, 27, 28, 29, 30, 31, 32], etc. Recently, it is being developed to investigate the trans- and supercritical fluid behaviors [33] or both the HNE and TNE simultaneously in complex systems [18, 34, 35, 36, 37, 38, 39, 40].[3] Such an LB kinetic model or discrete Boltzmann model (DBM) could bring

[3] As for Ref.[40], there is a typo on the sign in front of the correction term $\hat{A}_l$ in Eq.(1). It should be "−". The remaining derivations are correct.

some deeper insights into nonequilibrium behaviours in various complex fluids [18, 34, 35, 36, 37, 38, 39, 40, 41].

Previous LB models of combustion appear as a kind of new numerical scheme to solve the existing hydrodynamic models and work only for nearly incompressible systems with very low Mach number. Most of them assume that the chemical reaction does not affect the flow fields. To study the more practical cases, LB kinetic models for compressible flows [34, 38, 42, 43, 44] are needed. The first DBM for combustion and detonation was presented in 2013 [37], which works for 2-dimensional system in Cartesian coordinates. To probe the implosion and explosion processes, a polar coordinate DBM for combustion was formulated in 2014 [39]. Very recently, to make the specific heat ratio and Prandtl number flexible, we presented a multiple-relaxation-time DBM for combustion phenomena [40]. Some new observations on the complex detonation processes are obtained.

However, the three existing DBMs [37, 39, 40] for combustion are based only on a single distribution function. Consequently, they correspond to the hydrodynamic model where only one density is used. The separate descriptions of the reactant and product depend on a process parameter λ which is defined as the mass fraction of the product in the system. In this work we propose a double-distribution-function (DDF) DBM for combustion. Compared with the previous DBMs with single distribution function [37, 39, 40], this model can be used to study more details of the combustion, such as the variations of particle number density, particle mass density, flow velocity, internal energy, temperature, and pressure of each species. Another advantage of this model is its treatment of chemical reaction. The chemical reaction rate can be a function of the densities of the reaction and products, $F(\rho^A, \rho^B)$, rather than the chemical reaction process, $F(\lambda)$. The DDF DBM has the potential to describe a more real chemical reaction.

The rest of the paper is organized as follows. In Sec. 2 we formulate the DDF DBM based on a 2-dimensional 16-velocity discrete velocity model (D2V16 DVM). D2V13 and D2V17 DVMs are formulated for comparisons. Via the Chapman-Enskog multiscale analysis, the DDF DBM could recover reactive NS

equations. The Fick's first and second laws, Stefan-Maxwell diffusion equation are also successfully confirmed by this model. Section 3 displays the numerical simulations. Five benchmark tests are used to validate and verify the DBM. The physical accuracy of the coarse-grained model of the TNE and the computational costs of DBM based on various DVMs are discussed in Sec. 4. Section 5 summarizes the paper.

2. Model construction

To obtain more details of combustion procedure, we resort to DDF DBM. Recently, extensive efforts have been made to construct more accurate and stable models for multicomponent flows [45, 46, 47, 48, 49, 50, 51, 52, 53, 54, 55, 56, 57, 58, 59, 60, 61, 62, 63]. In 2001 Sofonea and Sekerka [49] proposed a nice Bhatnagar-Gross-Krook (BGK) model for isothermal binary fluid systems, where a split collision term model was discussed. In 2005 Xu [53] formulated a finite-difference LB method for the complete NS equations. This method is designed to simulate compressible and thermal binary fluid mixtures. However, previous DDF models can not describe compressible and thermal system with chemical reaction. In this work, we propose a DDF DBM for subsonic and supersonic combustion phenomena. This model is composed of two sets of equations. One set is two coupled discrete Boltzmann equations for thermal and high speed compressible fluid systems with two components, the other is a phenomenological equation for the chemical reaction process. Extension from a binary mixture DBM to a multispecies DBM appears straightforward [62, 63].

In this section, we first introduce the fundamental relations between the physical quantities and the (discrete) distribution functions. Those relations will be employed by the DDF DBM, which is obtained as a simple coarse-grained model. The DBM uses D2V16 model constructed in the following. Meanwhile, we present two other DVMs (D2V13 and D2V17), which will be used for comparisons. Finally, the NS equations, Fick's laws, and Stefan-Maxwell diffusion equation are recovered from the kinetic model.

2.1. Fluid system with two components

We consider a D-dimensional fluid system with two components. Particle of component σ ($= A$, B) has mass m^σ. The distribution function of component σ reads $f^\sigma \equiv f^\sigma(\mathbf{r}, \mathbf{v}, \eta^2)$ at the point ($\mathbf{r}$, $\mathbf{v}$, η) in phase space. The corresponding discrete function is $f_i^\sigma \equiv f_i^\sigma(\mathbf{r}, \mathbf{v}_i, \eta_i^2)$ with $i = 1, 2, \cdots, N$ and N the total number of the discrete velocities [4]. The particle number density, mass density and mean velocity of species σ are, respectively,

$$n^\sigma = \int\int f^\sigma d\mathbf{v} d\eta = \sum_i f_i^\sigma, \tag{1}$$

$$\rho^\sigma = m^\sigma n^\sigma, \tag{2}$$

$$\mathbf{u}^\sigma = \frac{1}{n^\sigma}\int\int f^\sigma \mathbf{v} d\mathbf{v} d\eta = \frac{1}{n^\sigma}\sum_i f_i^\sigma \mathbf{v}_i, \tag{3}$$

where the integral is extended over all phase space ($\mathbf{v}$,η). The particle number density, mass density and hydrodynamic velocity of physical system are

$$n = \sum_\sigma n^\sigma, \tag{4}$$

$$\rho = \sum_\sigma \rho^\sigma, \tag{5}$$

$$\mathbf{u} = \frac{1}{\rho}\sum_\sigma \rho^\sigma \mathbf{u}^\sigma, \tag{6}$$

respectively. The internal energy of species σ per unit volume and the internal energy of physical system are

$$E^\sigma = m^\sigma \int\int \frac{1}{2} f^\sigma [(\mathbf{v} - \mathbf{u})^2 + \eta^2] d\mathbf{v} d\eta = m^\sigma \sum_i \frac{1}{2} f_i^\sigma [(\mathbf{v}_i - \mathbf{u})^2 + \eta_i^2], \tag{7}$$

$$E = \sum_\sigma E^\sigma, \tag{8}$$

respectively. The energy equipartition theorem gives that

$$E = \frac{D + I}{2} nT, \tag{9}$$

[4] Because the discrete distribution function f_i depends on η_i^2, this model gives only the right physical quantities associated with the internal energies of extra DOFs, such as the specific heat ratio γ.

where I is the number of extra degrees of freedom (DOFs) [5], corresponding to molecular rotation and/or vibration, whose energy level is $\eta^2/2$. Consequently, the temperature of the whole system is

$$T = \frac{2E}{(D+I)n}. \tag{10}$$

Similarly, we define

$$\overline{T}^{\sigma} = \frac{2E^{\sigma}}{(D+I)n^{\sigma}} \tag{11}$$

as the temperature of species σ relative to the velocity $\mathbf{u}$ per unit volume. Here the overline of $\overline{T}^{\sigma}$ is used to distinguish from the definition in Eq. (B.11).

The local equilibrium distribution function $f^{\sigma eq}$ takes the form [64]

$$f^{\sigma eq} = n^{\sigma}\left(\frac{m^{\sigma}}{2\pi T}\right)^{D/2}\left(\frac{m^{\sigma}}{2\pi IT}\right)^{1/2}\exp\left[-\frac{m^{\sigma}(\mathbf{v}-\mathbf{u})^2}{2T} - \frac{m^{\sigma}\eta^2}{2IT}\right]. \tag{12}$$

It can be proved that $f^{\sigma eq}$ is the most probable distribution in the system with given parameters (m^{σ}, n^{σ}, $\mathbf{u}$, T, I). Furthermore, the definitions in Eqs. (1)−(12) are in line with the conservation of mass, momentum and energy.

2.2. Discrete Boltzmann equation

Our focus here is on the construction of a DBM suitable for combustion, but not on the chemical reaction mechanism. Since the chemical reaction is quite complex during the process of combustion. For convenience, the treatment of chemical reaction is simplified as follows:

1. The chemical reaction is irreversible and exothermic. No external force is under consideration. The electronic excitation, ionization and radiation are negligible. The combustion is temperature-dependent. The chemical reaction takes place when the temperature of chemical reactant $\overline{T}^{A}$ is larger than the ignition temperature T_c. This is a gross simplification. The ignition temperature

[5] In kinetic theory, the number of extra DOFs is a function of temperature, $I = I(T)$, and all DOFs are activated only at sufficiently high temperature. In this work, for simplicity, only a parameter η is used to globally describe the internal energies in extra DOFs, and I is constant. Its dependence upon temperature can be taken into account in future.

is an artificial input parameter. Other proper model including realistic chemical kinetics can also be employed. This was done, for example, by Karlin and co-authors [28, 29, 30].

2. We adopt the well known Cochran's rate function [65]

$$\lambda' = a_1 p^{a_2}(1-\lambda) + a_3 p^{a_4}\lambda(1-\lambda) \tag{13}$$

to describe the process of chemical reaction. Here the superscript $'$ is an operator denoting the material derivative $\frac{d}{dt}|_c$ on account of the effect of chemical reaction, i.e., $\lambda' = \frac{d\lambda}{dt}|_c$; And the mass fraction of product is $\lambda = \lambda^B = \rho^B/\rho$ with ρ^B the product density; The parameters a_1, a_2, a_3 and a_4 can be adjusted to control the rate of chemical reaction.

3. The chemical reaction time is much longer than that of the kinetic process but shorter than that of the hydrodynamic flow behavior [9]. Therefore, during a relatively short period of the local chemical reaction, neither mass density of physical system nor hydrodynamic velocity of the system is affected when the temperature changes with the chemical energy transformed into heat.

With the aforementioned conditions, we get the following discrete Boltzmann equation,

$$\frac{\partial f_i^\sigma}{\partial t} + v_{i\alpha}\frac{\partial f_i^\sigma}{\partial r_\alpha} = \Omega_i^\sigma + C_i^\sigma, \tag{14}$$

where the superscript $\sigma = A$ denotes the reactant and B the product; f_i^σ is the discrete nonequilibrium distribution function of component σ; $v_{i\alpha}$ $(= v_{ix},\ v_{iy})$ the discrete velocity; r_α $(= x,\ y)$ the coordinate $(D = 2)$. The collision term Ω_i^σ is given as

$$\Omega_i^\sigma = -\frac{1}{\tau^\sigma}(f_i^\sigma - f_i^{\sigma eq}), \tag{15}$$

where $f_i^{\sigma eq}$ is the discrete equilibrium distribution function of component σ; The relaxation time is $\tau^\sigma = 1/(n^A/\theta^A + n^B/\theta^B)$, with two relaxation parameters θ^A and θ^B to be determined [49]. To assure local momentum conservation, the relaxation time of the two components should be equal to each other [49], i.e., $\tau^\sigma = \tau$. The chemical term is written as

$$C_i^\sigma = \frac{1}{\tau^\sigma}(f_i^{\sigma * eq} - f_i^{\sigma eq}), \tag{16}$$

where $f_i^{\sigma eq} = f_i^{\sigma eq}(n^\sigma, \mathbf{u}, T)$ and $f_i^{\sigma * eq} = f_i^{\sigma * eq}(n^{\sigma *}, \mathbf{u}, T^*)$ represent the equilibrium distribution function before and after chemical reaction, respectively. The physical quantities after reaction are

$$\rho^{\sigma *} = \rho^\sigma + \rho \lambda^{\sigma \prime} \tau^\sigma, \tag{17}$$

$$n^{\sigma *} = \frac{\rho^{\sigma *}}{m^\sigma}, \tag{18}$$

$$n^* = \sum_\sigma n^{\sigma *}, \tag{19}$$

$$E^* = E + \rho \lambda' Q \tau^\sigma, \tag{20}$$

$$T^* = \frac{2E^*}{(D+I)n^*}, \tag{21}$$

where Q is the amount of heat released by the chemical reactant per unit mass; $\lambda^\sigma (= \rho^\sigma / \rho)$ is the mass fraction of species σ. It is clear that $\lambda^B = 1 - \lambda^A$ and $\lambda^{B\prime} = -\lambda^{A\prime}$.

From Eqs. (9) and (20), we get

$$E' = \rho \lambda' Q = E'_T + E'_n, \tag{22}$$

with

$$E'_T = \frac{D+I}{2} n' T = \frac{D+I}{2} \frac{dn}{dt}|_c T, \tag{23}$$

$$E'_n = \frac{D+I}{2} n T' = \frac{D+I}{2} \frac{dT}{dt}|_c n, \tag{24}$$

where E'_T (E'_n) is the energy for the increase of particle number density (temperature) with fixed temperature (particle number density). When $Q = 0$, we get $E'_T + E'_n = 0$ and $n'/T' = -n/T$.

Equations (17)$-$(20) give

$$n' = \sum_\sigma n^{\sigma \prime} = -\sum_\sigma \frac{\rho \lambda'}{m^\sigma}, \tag{25}$$

$$E' = \rho Q \lambda'. \tag{26}$$

From Eqs. (10), (25) and (26), we get

$$T' = (\frac{2}{D+I} \frac{E}{n})' = \frac{\rho \lambda'}{n} (\frac{2Q}{D+I} - \frac{m^A - m^B}{m^A m^B} T). \tag{27}$$

Consequently, the temperature increases under the condition

$$Q > \frac{D+I}{2}\frac{m^A - m^B}{m^A m^B}T, \tag{28}$$

otherwise, it does not increase. When $Q = 0$, the temperature reduces (increases) in the process of decomposition (combination) reaction.

In addition, the temporal derivative in discrete Boltzmann equation (14) is solved analytically with the first order accuracy [38], the spatial derivative in Eq. (14) is calculated by adopting the nonoscillatory and nonfree-parameters dissipative finite difference scheme with the second order accuracy [66], and the chemical term (16) is calculated with the first order accuracy. Note that, at the level of the first order accuracy, the chemical term (16) is equivalent to the one proposed in our previous work [40]. In fact, both this model and the previous one [40] are limited to the first order accuracy. Furthermore, the method used here is different from that used in our previous works [37, 39, 40] to couple the chemical reaction with the flow behaviors. In our previous works [37, 39, 40], λ is obtained by solving the semiempirical evolution equation. While in this work, the result of λ is directly given by its definition $\lambda = \rho^B/\rho$. The latter approach is more reliable. Moreover, compared with the chemical term calculated in Ref. [40] using 24 discrete velocities, the chemical term given by Eq. (16) allows the DBM to employ less discrete velocities, see the following subsection. That is to say, the method presented here is more efficient.

2.3. Discrete velocity model

Here we present three DVMs, i.e., D2V16, D2V13, and D2V17. The number of discrete velocities in the three DVMs is $N = 16$, 13, and 17, respectively. The first DVM works for the case where the specific heat ratio γ is adjustable, and the last two only for the case of fixed $\gamma = 2$. The discrete equilibrium distribution function should satisfy the following moment relations

$$\mathbf{M}\ \mathbf{f}^{\sigma eq} = \hat{\mathbf{f}}^{\sigma eq}, \tag{29}$$

where $\mathbf{f}^{\sigma eq} = (f_1^{\sigma eq}, f_2^{\sigma eq}, \cdots, f_N^{\sigma eq})^T$ is a set of discrete equilibrium distribution function; $\hat{\mathbf{f}}^{\sigma eq} = (\hat{f}_1^{\sigma eq}, \hat{f}_2^{\sigma eq}, \cdots, \hat{f}_N^{\sigma eq})^T$ is a set of moments provided by the

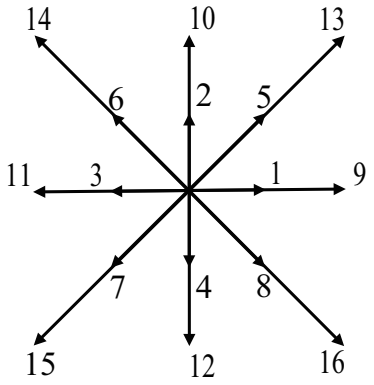

Figure 1: Schematic of the D2V16 model.

discrete equilibrium distribution function; And $\mathbf{M} = (\mathbf{M}_1, \mathbf{M}_2, \cdots, \mathbf{M}_N)^T$ is a $N \times N$ matrix that acts as a bridge between $\mathbf{f}^{\sigma eq}$ and $\hat{\mathbf{f}}^{\sigma eq}$, with $\mathbf{M}_i = (m_{i1}, m_{i2}, \cdots, m_{iN})$. It should be pointed out that the moment relations in Eq. (29) are chosen to recover the hydrodynamic equations. And the number of discrete velocities in each DVM equals that of the relations in Eq. (29). From Eq. (29), we get the discrete equilibrium distribution functions as

$$\mathbf{f}^{\sigma eq} = \mathbf{M}^{-1}\hat{\mathbf{f}}^{\sigma eq}, \tag{30}$$

where $\mathbf{M}^{-1}$ is the inverse matrix of $\mathbf{M}$.

The specific elements of $\hat{\mathbf{f}}^{\sigma eq}$ and $\mathbf{M}$ in D2V16, D2V13, and D2V17 are summarized in Appendix A. The discrete velocities $\mathbf{v}_i$ in the three DVMs are listed in Table 1. The elements η_i in D2V16 are (η_1, η_2, ..., η_N) = (0, 0, 0, 0, η_a, η_a, η_a, η_a, 0, 0, 0, 0, 0, 0, 0, 0). The schematic of D2V16 is shown in Fig. 1.

Remark: (I) The parameters (v_a, v_b, v_c, v_d, η_a) in D2V16, (v_a, v_b, v_c, v_d, v_e) in D2V13, or (v_a, v_b, v_c, v_d, v_e, v_f) in D2V17 can be adjusted to optimize the properties of the model. Their values should guarantee the existence of $\mathbf{M}^{-1}$. (II) The 16 (13) relations in D2V16 (D2V13) are the necessary and sufficient conditions for the recovery of NS equations with flexible γ (fixed $\gamma = 2$), via

DVM	$\begin{pmatrix} v_{1x}, v_{2x}, \ldots, v_{Nx} \\ v_{1y}, v_{2y}, \ldots, v_{Ny} \end{pmatrix}$
D2V16	$\begin{pmatrix} v_a, 0, -v_a, 0, v_b, -v_b, -v_b, v_b, v_c, 0, -v_c, 0, v_d, -v_d, -v_d, v_d \\ 0, v_a, 0, -v_a, v_b, v_b, -v_b, -v_b, 0, v_c, 0, -v_c, v_d, v_d, -v_d, -v_d \end{pmatrix}$
D2V13	$\begin{pmatrix} v_a, 0, -v_a, 0, v_b, -v_b, -v_b, v_b, v_c, 0, -v_c, 0, v_d \\ 0, v_a, 0, -v_a, v_b, v_b, -v_b, -v_b, 0, v_c, 0, -v_c, v_e \end{pmatrix}$
D2V17	$\begin{pmatrix} v_a, 0, -v_a, 0, v_b, -v_b, -v_b, v_b, v_c, 0, -v_c, 0, v_d, -v_d, -v_d, v_d, v_e \\ 0, v_a, 0, -v_a, v_b, v_b, -v_b, -v_b, 0, v_c, 0, -v_c, v_d, v_d, -v_d, -v_d, v_f \end{pmatrix}$

Table 1: Discrete velocities in D2V16, D2V13, and D2V17.

the Chapman-Enskog expansion. While D2V17 contains another 4 relations in addition to the 13 ones in D2V13 needed for the recovery of NS equations with fixed $\gamma = 2$. (III) Theoretically, the discrete (equilibrium) distribution function f_i^σ ($f_i^{\sigma eq}$) contains more information in D2V17 than that in D2V13. Because there are more moment relations satisfied by $f_i^{\sigma eq}$ in D2V17 than those in D2V13. More physical quantities could be obtained from the DVM with more relations. (IV) The computational efficiency of D2V17 is lower than that of D2V13, because there are more discrete velocities in D2V17 than those in D2V13. (V) Compared with D2V33 [67] and D2V65 [64], the D2V13 (or D2V17) and D2V16 can be used to recover the same NS equations with fixed and flexible specific heat ratio, respectively. But both the latter have much less discrete velocities than the former.

2.4. Kinetic properties of DBM

It is easy to prove that, via the Chapman-Enskog expansion, this model could recover the reactive NS equations in the hydrodynamic limit

$$\frac{\partial \rho^\sigma}{\partial t} + \frac{\partial}{\partial r_\alpha}(\rho^\sigma u_\alpha^\sigma) = \rho \lambda^{\sigma\prime}, \tag{31}$$

$$\begin{aligned} &\frac{\partial}{\partial t}(\rho^\sigma u_\alpha^\sigma) + \frac{\partial}{\partial r_\beta}(\delta_{\alpha\beta} p^\sigma + \rho^\sigma u_\alpha^\sigma u_\beta^\sigma) + \frac{\partial}{\partial r_\beta}(P_{\alpha\beta}^\sigma + U_{\alpha\beta}^\sigma + V_{\alpha\beta}^\sigma) \\ &= \rho u_\alpha \lambda^{\sigma\prime} - \frac{\rho^\sigma}{\tau^\sigma}(u_\alpha^\sigma - u_\alpha), \end{aligned} \tag{32}$$

$$\frac{\partial}{\partial t}[\rho^\sigma(e^\sigma+\frac{1}{2}u^{\sigma 2})]+\frac{\partial}{\partial r_\alpha}[\rho^\sigma u_\alpha^\sigma(e^\sigma+\frac{1}{2}u^{\sigma 2})+p^\sigma u_\alpha^\sigma]$$
$$-\frac{\partial}{\partial r_\alpha}[\kappa^\sigma\frac{\partial}{\partial r_\alpha}(\frac{D+I}{2}\frac{T^\sigma}{m^\sigma})-u_\beta^\sigma P_{\alpha\beta}^\sigma+X_\alpha^\sigma+Y_\alpha^\sigma+Z_\alpha^\sigma]$$
$$=\rho\lambda^{\sigma\prime}(\frac{D+I}{2}\frac{T}{m^\sigma}+\frac{1}{2}u^2)+\frac{D+I}{2}\frac{\rho^\sigma}{m^\sigma}\frac{\rho\lambda'}{n}(\frac{2Q}{D+I}-\frac{m^A-m^B}{m^Am^B}T)$$
$$-\frac{\rho^\sigma}{\tau^\sigma}(\frac{D+I}{2}\frac{T^\sigma}{m^\sigma}+\frac{1}{2}u^{\sigma 2}-\frac{D+I}{2}\frac{T}{m^\sigma}-\frac{1}{2}u^2), \tag{33}$$

with

$$P_{\alpha\beta}^\sigma=-\mu^\sigma(\frac{\partial u_\alpha^\sigma}{\partial r_\beta}+\frac{\partial u_\beta^\sigma}{\partial r_\alpha}-\frac{2\delta_{\alpha\beta}}{D+I}\frac{\partial u_\chi^\sigma}{\partial r_\chi}), \tag{34}$$

$$U_{\alpha\beta}^\sigma=-\rho^\sigma[\frac{\delta_{\alpha\beta}}{D+I}(u^{\sigma 2}+u^2-2u_\chi^\sigma u_\chi)+u_\alpha u_\beta^\sigma+u_\alpha^\sigma u_\beta-u_\alpha^\sigma u_\beta^\sigma-u_\alpha u_\beta], \tag{35}$$

$$V_{\alpha\beta}^\sigma=\frac{\lambda^{\sigma\prime}}{\lambda^\sigma}\tau^\sigma U_{\alpha\beta}^\sigma, \tag{36}$$

$$X_\alpha^\sigma=\tau^\sigma(D+I+2)\frac{\rho^\sigma(u_\alpha^\sigma-u_\alpha)}{m^\sigma}\frac{\rho\lambda'}{n}(\frac{Q}{D+I}-\frac{m^A-m^B}{2m^Am^B}T), \tag{37}$$

$$Y_\alpha^\sigma=\frac{\rho^\sigma u_\alpha^\sigma}{D+I}(u_\beta^\sigma-u_\beta)^2+\rho^\sigma(u_\alpha^\sigma-u_\alpha)(-\frac{D+I+2}{2}\frac{T^\sigma-T}{m^\sigma}-\frac{1}{2}u^{\sigma 2}+\frac{1}{2}u^2), \tag{38}$$

$$Z_\alpha^\sigma=\frac{\lambda^{\sigma\prime}}{\lambda^\sigma}\tau^\sigma Y_\alpha^\sigma, \tag{39}$$

where $p^\sigma=n^\sigma T^\sigma$, $e^\sigma=(D+I)T^\sigma/(2m^\sigma)$, $\mu^\sigma=p^\sigma\tau^\sigma$, and $\kappa=\gamma\mu^\sigma$ are the pressure, the internal energy per unit mass, the dynamic viscosity coefficient, and heat conductivity of species σ, respectively; $\gamma=(D+I+2)/(D+I)$ is the specific heat ratio.

Performing the operator $\sum_\sigma$ to the two sides of Eqs. (31) − (33) gives the reactive NS equations describing the whole system,

$$\frac{\partial\rho}{\partial t}+\frac{\partial}{\partial r_\alpha}(\rho u_\alpha)=0, \tag{40}$$

$$\frac{\partial}{\partial t}(\rho u_\alpha)+\frac{\partial}{\partial r_\beta}\sum_\sigma(\delta_{\alpha\beta}p^\sigma+\rho^\sigma u_\alpha^\sigma u_\beta^\sigma)+\frac{\partial}{\partial r_\beta}\sum_\sigma(P_{\alpha\beta}^\sigma+V_{\alpha\beta}^\sigma)=0, \tag{41}$$

$$\frac{\partial}{\partial t}[\rho(e+\frac{1}{2}u^2)]+\frac{\partial}{\partial r_\alpha}[\sum_\sigma\rho^\sigma u_\alpha^\sigma(e^\sigma+\frac{1}{2}u^{\sigma 2})+p^\sigma u_\alpha^\sigma]$$
$$-\frac{\partial}{\partial r_\alpha}\sum_\sigma[\kappa^\sigma\frac{\partial}{\partial r_\alpha}(\frac{D+I}{2}\frac{T^\sigma}{m^\sigma})-u_\beta^\sigma P_{\alpha\beta}^\sigma+Y_\alpha^\sigma+Z_\alpha^\sigma]=\rho\lambda' Q, \tag{42}$$

where the internal energy of the whole system per unit mass $e = \sum_\sigma \rho^\sigma (e^\sigma + u^{\sigma 2}/2)/\rho - u^2/2$.

For the isothermal system without chemical reaction, when the relative flow velocity between the two species is small, we have $T^\sigma = T$, $\lambda^{\sigma\prime} = 0$, and $u^\sigma \approx u$. Then Eq. (41) is equivalent to

$$\frac{\partial}{\partial t}(\rho u_\alpha) + \frac{\partial}{\partial r_\beta}(\delta_{\alpha\beta} p + \rho u_\alpha u_\beta) + \frac{\partial P_{\alpha\beta}}{\partial r_\beta} = 0, \tag{43}$$

where

$$p = \sum_\sigma p^\sigma = nT, \tag{44}$$

$$P_{\alpha\beta} = \sum_\sigma P^\sigma_{\alpha\beta} = -\mu(\frac{\partial u_\alpha}{\partial r_\beta} + \frac{\partial u_\beta}{\partial r_\alpha} - \frac{2\delta_{\alpha\beta}}{D+I}\frac{\partial u_\chi}{\partial r_\chi}), \tag{45}$$

with the dynamic viscosity coefficient of the whole system

$$\mu = p\tau. \tag{46}$$

In addition, it is easy to demonstrate [52, 56, 68, 69] that Fick's first law

$$J^\sigma_\alpha = -D^\sigma \frac{\partial \rho^\sigma}{\partial r_\alpha}, \tag{47}$$

Fick's second law

$$\frac{\partial \lambda^\sigma}{\partial t} = D^\sigma \frac{\partial}{\partial r_\alpha}(\frac{\partial \lambda^\sigma}{\partial r_\alpha}), \tag{48}$$

and Stefan-Maxwell diffusion equation

$$M^A M^B (u^B_\alpha - u^A_\alpha) = D\frac{\partial M^A}{\partial r_\alpha} - D(\lambda^A - M^A)\frac{1}{p}\frac{\partial p}{\partial r_\alpha}, \tag{49}$$

can be derived from the DBM. Here $J^\sigma_\alpha = \rho^\sigma(u^\sigma_\alpha - u_\alpha)$ is the diffusive flux of mass relative to local barycentric velocity field, $D^\sigma = \tau^\sigma T/m^\sigma$ the diffusivity of species σ, $M^\sigma = n^\sigma/n$ the mole fraction, and

$$D = \frac{\rho}{\rho^A \rho^B} M^A M^B p\tau \tag{50}$$

the diffusion coefficient of the whole system. From Eqs. (46) and (50), we obtain the Schmidt number of the whole system

$$Sc = \frac{\mu}{\rho D} = \frac{\rho^A \rho^B}{M^A M^B \rho^2}. \tag{51}$$

Obviously, the Schmidt number of each species is $Sc^{\sigma} = 1$ in the self-diffusion case, which is typical for gases [49].

Furthermore, the DBM has some intrinsic advantages over conventional NS method. For instance, (i) NS equations include nonlinear convection terms, while LB equation is in a uniformly linear form and its algorithm is easy to code. (ii) NS method often involves the solution of Poisson equation, which requires global data communication. While all the information transfer in DBM is local in time and space, so it is suitable for massively parallel computers. (iii) The DBM provides a simple method of nonequilibrium investigation, by means of calculating the velocity moments of discrete (equilibrium) distribution functions, see Appendix B. In contrast, by combining the hydrodynamic equations (such as NS equations) and the evolution equations of nonequilibrium manifestations, the nonequilibrium investigation may also be made. However, it is bound to be difficult and complex, see Appendix B. Although the computation costs of DVM are higher than hydrodynamic formulations, the computational overhead is minor on account of its advantages.

3. Numerical simulations

The validation and verification of the model are performed in this section, which is divided into five parts. The first three parts are 1-dimensional phenomena, the last two parts are 2-dimensional phenomena. Part one is an isothermal binary diffusion. Parts two and three show simulations of combustion in two different cases. Specifically, part two is for the case without reaction heat released. Part three is for a steady detonation. In the fourth part, we simulate the Kelvin-Helmholtz instability (KHI) without chemical reaction. Finally, we conduct a simulation of the Richtmyer-Meshkov instability (RMI) induced by a detonation wave. It should be mentioned that only D2V16 is used in this section.

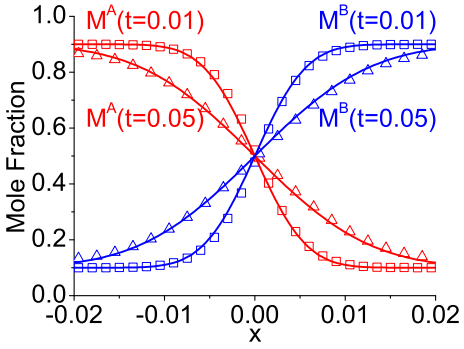

Figure 2: Mole fractions M^A and M^B in the binary diffusion at two instants: $t = 0.01$ and 0.05. Symbols denote DBM simulation results and continuous lines denote the corresponding analytical solutions.

3.1. Binary diffusion

Diffusion takes place when two miscible species are brought into contact. It plays an important role in combustion [70]. The evolution of macroscopic concentration of each species obeys Fick's law. For isothermal diffusion, the following analytical solution works

$$M^\sigma = [\frac{1}{2} + \frac{\Delta M^\sigma}{2} erf(\frac{x}{\sqrt{4Dt}})], \tag{52}$$

where ΔM^σ is the initial mole fraction difference and D the diffusion coefficient. To compare with this solution, we simulate an isothermal diffusion here. The mixture of the two gases is initially given by the following step function,

$$\begin{cases} (M^A, M^B)_L = (90\%, 10\%), \\ (M^A, M^B)_R = (10\%, 90\%), \end{cases}$$

where the suffix L indexes the left part and R the right part along the axial direction x. It is remarked that the use of step function is generally regarded as a difficult test for the code compared to the use of smooth profiles [56]. The molecular masses are $m^A = m^B = 1$, the relaxation parameters $\theta^A = \theta^B = 10^{-3}$, and the other parameters $I = 0$, $(v_a, v_b, v_c, v_d, \eta_a) = (0.6, 1.0, 1.5, 3.5, 1.1)$, $\Delta t = 10^{-5}$, $\Delta x = \Delta y = 5 \times 10^{-4}$, $N_x \times N_y = 80 \times 1$.

Figure 2 shows the comparison of mole fractions of the two species between the DBM simulation results and the analytical solution with $\Delta M^{\sigma} = 0.8$ and $D = 10^{-3}$. The simulation results at constants $t = 0.01$ and 0.05 are denoted by squares and triangles, respectively. The corresponding analytical solutions are denoted by lines. Figure 2 shows a satisfying agreement between the two results. Furthermore, for the same initial concentration difference, it is possible to obtain a molecular mass ratio as large as $m^A : m^B = 2000 : 1$. It is confirmed that the DBM has a good capability of describing the interaction between two species.

3.2. Steady shock

Let us consider a detonation wave without chemical energy released during reaction, so it reduces to a shock wave [4, 71]. Now we perform the simulation in such case. The ignition temperature is $T_c = 1.3$. The parameters $a_1 = 1$, $a_2 = 1$, $a_3 = 200$, and $a_4 = 1$ are given here to control the chemical reaction. The initial physical quantities read

$$\begin{cases} (\rho, u_x, u_y, p, \lambda)_L = (2.18182, 1.08333, 0, 3.16667, 1), \\ (\rho, u_x, u_y, p, \lambda)_R = (1, 0, 0, 1, 0), \end{cases}$$

with L designating $0 \leq x < 0.1$ and R designating $0.1 \leq x < 1.0$. The quantities at the two parts satisfy Hugoniot relations for shock wave. Other parameters are $I = 3$, $(v_a,\ v_b,\ v_c,\ v_d,\ \eta_a) = (1.9,\ 1.2,\ 2.5,\ 3.3,\ 3.3)$, $\theta^A = 10^{-3}$, $\theta^B = 5 \times 10^{-4}$, $N_x \times N_y = 1000 \times 1$, $\Delta x = \Delta y = 10^{-3}$, $\Delta t = 10^{-4}$.

Figure 3 plots physical quantities $(\rho,\ u_x,\ p)$ in the case of steady shock with various mass ratios at time $t = 0.3$. The DBM simulation results are denoted by symbols (squares for the case $m^A = 1.0$ and $m^B = 1.0$, circles for $m^A = 1.0$ and $m^B = 1.5$, and triangles for $m^A = 1.2$ and $m^B = 1.0$), the analytical solution by continuous lines. It is clear to find in Fig. 3 that the simulation results have a satisfying agreement with the theoretical ones.

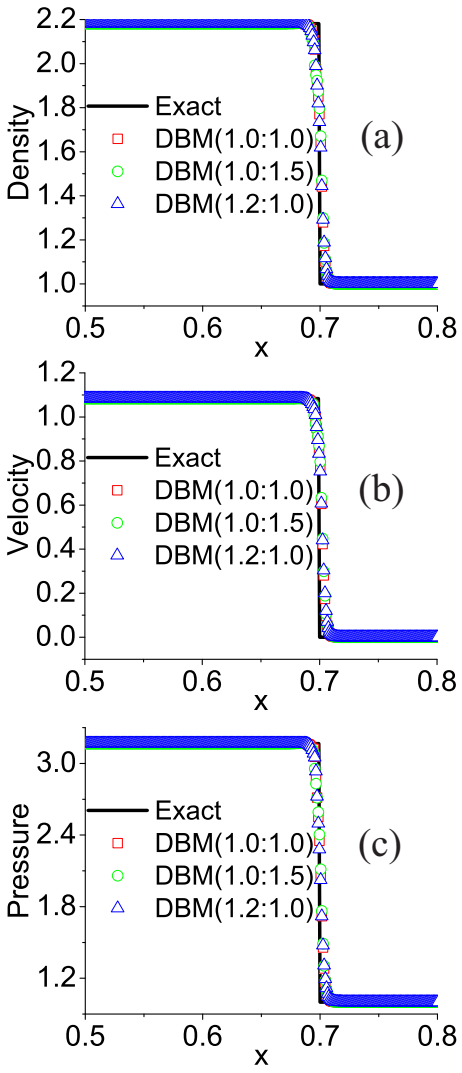

Figure 3: Profiles of steady shock at time $t = 0.3$: (a) mass density, (b) velocity u_x, (c) pressure. The analytical solution and the DBM simulation results in various cases of mass ratio $m^A : m^B$ are given in each panel. The continuous lines denote analytical solutions. The squares are for the simulation results of mass ratio $m^A : m^B = 1.0 : 1.0$, the circles for $1.0 : 1.5$, and the triangles for $1.2 : 1.0$.

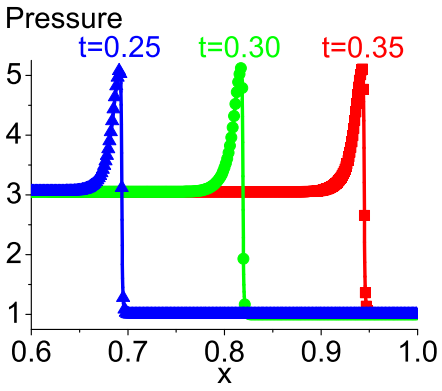

Figure 4: The pressure along $x-$axis in the evolution of steady detonation at various instants: $t = 0.25$, 0.30, and 0.35 from left to right, respectively.

3.3. Steady detonation

Realistically, there is a large amount of heat released in the process of combustion or detonation in most cases, and the heat can make combustion or detonation self-sustaining [4]. As a simple example, a steady detonation is simulated here with the released reaction heat $Q = 2.0$ and Mach number 2.12643. The parameters $T_c = 1.6$, $a_1 = 1$, $a_2 = 1$, $a_3 = 100$ and $a_4 = 1$ are given here to control the chemical reaction. The initial physical quantities read

$$\begin{cases} (\rho, u_x, u_y, p, \lambda)_L = (1.48043, 0.816497, 0, 3.05433, 1), \\ (\rho, u_x, u_y, p, \lambda)_R = (1, 0, 0, 1, 0). \end{cases}$$

The quantities above satisfy Hugoniot relations for detonation wave. Other parameters are $m^A = 1.5$, $m^B = 1$, $I = 3$, $(v_a,\ v_b,\ v_c,\ v_d,\ \eta_a) = (1.9,\ 1.6,\ 3.2,\ 6.9,\ 3.9)$, $\theta^A = 2 \times 10^{-4}$, $\theta^B = 10^{-4}$, $N_x \times N_y = 5000 \times 1$, $\Delta x = \Delta y = 2 \times 10^{-4}$, $\Delta t = 2 \times 10^{-5}$.

Figure 4 gives the simulation results of pressure along $x-$axis in the evolution of the steady detonation. The results at various instants $t = 0.25$, 0.30, and 0.35 are given from left to right, respectively. It can be found in Fig. 4 that the three profiles are similar to each other, which means the occurrence of a steady detonation wave. Our simulation results show that the detonation velocity is 2.512, and the analytic solution is 2.516. The relative error is about 0.16%.

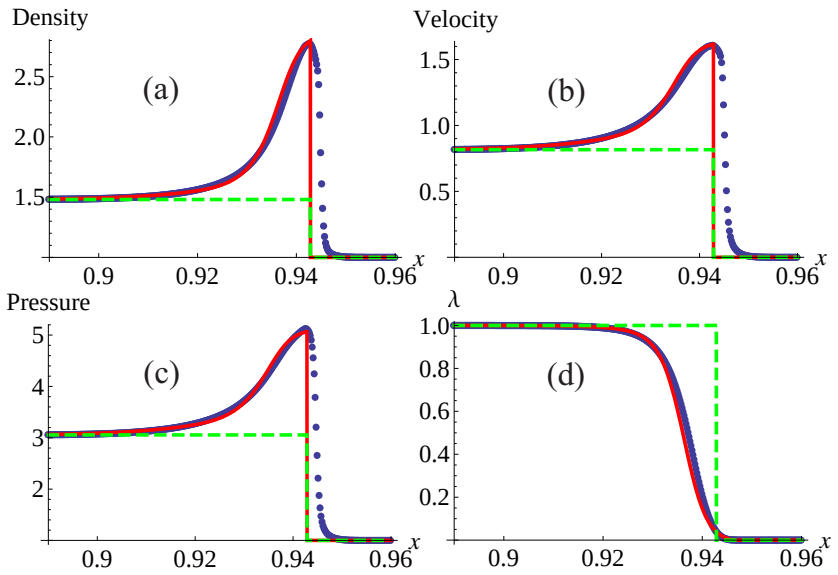

Figure 5: Physical quantities of steady detonation at time $t = 0.35$: (a) particle mass density ρ, (b) horizontal velocity u_x, (c) pressure p, (d) λ. The solid circles denote DBM simulation results, the continuous lines ZND solutions, the dashed lines CJ solutions.

Figure 5 illustrates the comparison between the simulation results and the analytical resolutions of physical quantities (ρ, u_x, p, λ) in the evolution of steady detonation at time $t = 0.35$. The solid circles are for the simulation results, the continuous lines for the analytic solutions of ZND theory [4, 72, 73, 74], and the dashed lines for CJ theory [4, 75, 76]. The simulation results in the detonation wave back are $\rho = 1.48077$, $u_x = 0.816470$, $p = 3.05400$, $\lambda = 1.0$. The deviations of them from the theoretical results are about 0.02%, 0.0%, 0.01%, 0.0%, respectively. Obviously, the simulation results have a satisfying agreement with the theoretical ones. Furthermore, it can be found that the DBM simulation results agree well with the ZND results behind the von Neumann peak. And there are a few differences between them in front of the von Neumann peak. In fact, the ZND theory ignores the viscosity and heat conduction, and it simply gives a strong discontinuity at the von Neumann peak. Therefore, it is not accurate enough. While our simulation includes the effects of viscosity, heat conduction and other kinds of relevant transportation [39]. In short, the current model has the capability of simulating detonation. Further test demonstrates that the current model is successfully used to simulate detonation problem with Mach number 7.5 (not shown here).

Moreover, compared with the previous kinetic models with single distribution function [37, 39, 40], this model gives the same accuracy in predicting the ZND structure, since all of them are limited at the level of the first order accuracy. And this model can be used to study more details of the detonation structure, such as the variations of particle number density, particle mass density, flow velocity, internal energy, temperature, and pressure of each species (not shown here). Another advantage of this model is its treatment of chemical reaction. The chemical reaction rate can be connected with the densities of the reaction and products rather than a parameter λ. The DDF DBM has the capability to describe a more real chemical reaction.

3.4. Kelvin-Helmholtz instability

The KHI occurs when there is a relative tangential motion between two fluids with different physical parameters [77]. It plays an essential role in various situations, such as the wind blowing over the ocean, the stream structure of solar corona, the helical wave motion in ionized comet tails, the meteor entering the Earth's atmosphere, the Eagle Nebula in astrophysics, the ignition in inertial confinement fusion, the reacting mixing layers in combustion [78]. Here we simulate the KHI phenomenon which is a typical 2-dimensional complex problem. The initial physical field is given as follows

$$\begin{cases} n^{\sigma}(x) = \frac{n_L^{\sigma}+n_R^{\sigma}}{2} - \frac{n_L^{\sigma}-n_R^{\sigma}}{2}\tanh(\frac{x-x_0+W\cos(ky)}{D_{\rho}}), \\ \mathbf{u}(x) = \frac{\mathbf{u}_L+\mathbf{u}_R}{2} - \frac{\mathbf{u}_L-\mathbf{u}_R}{2}\tanh(\frac{x-x_0+W\cos(ky)}{D_u}), \\ p(x) = p_L = p_R, \end{cases}$$

where n_L^{σ} (n_R^{σ}) is the particle number density of species σ near the left (right) boundary; $\mathbf{u}_L$ and p_L ($\mathbf{u}_R$ and p_R) are the velocity and pressure of the system near the left (right) boundary, respectively; D_{ρ} (D_u) is the width of density (velocity) transition layer; x_0 is the averaged x position of material interface; W is the amplitude of initial perturbation imposed on the physical field; k the perturbation wave number. The two species have the same initial velocity and temperature at the same points. Furthermore, boundary conditions for the simulation of KHI are as follows: the outflow (zero gradient) boundary conditions are adopted in the x direction, the periodic boundary conditions in the y direction. The parameters are chosen as $n_L^A = 0.8$, $n_R^A = 0.2$, $n_L^B = 0.2$, $n_R^B = 0.8$, $\mathbf{u}_L = u_L\mathbf{e}_y$, $\mathbf{u}_R = u_R\mathbf{e}_y$, $u_L = 0.5$, $u_R = -0.5$, $D_u = 5\Delta x$, $D_{\rho} = 5\Delta x$, $W = 4\Delta x$, $x_0 = 0.05$, $k = 20\pi$, $\theta^A = 10^{-5}$, $\theta^B = 5\times10^{-6}$, $\Delta t = 5\times10^{-6}$, $\Delta x = \Delta y = 5\times10^{-4}$, $N_x \times N_y = 200\times200$.

Figure 6 shows the density contours in the evolution of KHI at $t = 0.00$, 0.05, 0.15, and 0.30, respectively. Figure 6 (a) shows the initial density field where two fluids are divided by a single-mode sinusoidal perturbed interface. From Figs. 6 (a)−(b) we can find that the interface starts to wiggle due to the initial perturbation and the velocity shear. Figures 6 (b)−(c) show that it rolls

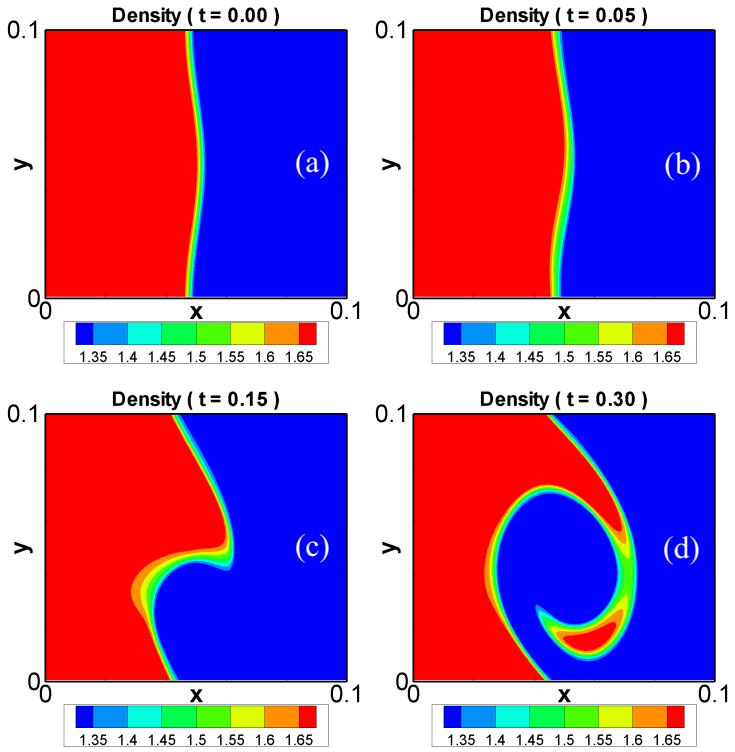

Figure 6: Density contours in the evolution of KHI at instants $t = 0.00$, 0.05, 0.15, and 0.30, respectively

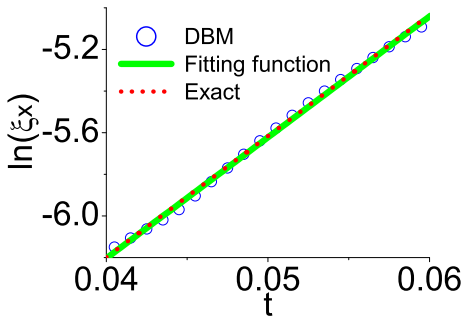

Figure 7: The results of ξ_x versus time t in the linear stage of KHI.

up gradually on account of the KHI effect. It is clear to get from Figs. 6 (c)−(d) that the interfacial deformation becomes more and more significant. A larger vortex rotation is clearly observed at time $t = 0.30$. From the evolution of the continuous and smooth interface in Fig. 6, it is confirmed that, the model has a good ability of capturing interface deformation.

To quantitatively compare the simulation results with the analytical solution, we show the logarithm of the perturbed peak kinetic energy $\xi_x = \rho u_x^2$ versus time t in the evolution of KHI, see Fig. 7. The profile of $\ln(\xi_x)$ within the linear stage ($0.04 < t < 0.06$) of the KHI is plotted. The circles represent the simulation results, the continuous line denotes the fitting function $F(t) = -8.53032 + 58.1616\ t$, and the dashed line is for the analytical solution $F(t) = -8.53032 + 2\dot{A}\ t$ where $\dot{A} = 29.1392$ is half linear growth rate of ξ_x [43]. The explicit analytic formula of $\dot{A}$ is given by Eq. (18) in Ref. [79]. It is found that the relative difference of $\dot{A}$ between the fitting function and the analytical solution is 0.20%, which is satisfying.

In order to capture the frequency ω in the evolution of KHI, we define the following correlation function

$$\varphi(L, t_1, t_2) = \int\int \rho(x, y, t_1)\rho(x, y + L, t_2)dxdy \tag{53}$$

where $\rho(x, y, t_1)$ and $\rho(x, y, t_2)$ denote the density field at times t_1 and t_2, respectively. The maximum of $\varphi(L, t_1, t_2)$ within $0 \leq L < 0.1$ is located around

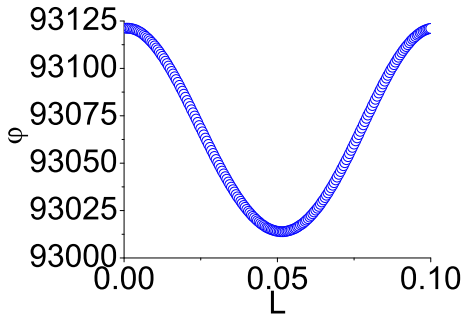

Figure 8: The distribution of $\varphi(L, 5\times10^{-2}, 6\times10^{-2})$ versus parameter L.

$\overline{u_y}(t_2 - t_1)$, where $\overline{u_y}$ is the average vertical velocity of the density field at time $(t_1 + t_2)/2$. Then the frequency is obtained

$$\omega = k\overline{u_y}. \tag{54}$$

Figure 8 shows the distribution of $\varphi(L, t_1, t_2)$ versus L with $t_1 = 5\times10^{-2}$ and $t_2 = 6\times10^{-2}$. The maximum of φ is located at $L = 10^{-3}$. Consequently, we obtain $\overline{u_y} = 0.1$ and $\omega = 6.28$ at $t = 5.5\times10^{-2}$. The analytical solution calculated by Eq. (19) in Ref. [79] is $\omega = 5.60551$. The difference between the DBM and the analytical solution mainly results from numerical errors. From $L = 10^{-3}$ and $\Delta y = 5\times10^{-4}$, we find that the flow moves upward with only $L/\Delta y = 2$ space steps. To reduce the numerical errors, we can decrease the space step. A further study is beyond this work.

3.5. Richtmyer-Meshkov instability

The RMI [80, 81] occurs when a shock travels across a corrugated interface separating two fluids with different thermodynamic properties. The interplay between a shock and a flame is commonplace in many combustion systems, and the resulting instability plays a significant role in combustion [82]. To simulate such a phenomenon, we give the initial configuration as below

$$\begin{cases} (\rho, u_x, u_y, p, \lambda)_L &= (1.38837, 0.57735, 0, 2.19162, 1), \\ (\rho, u_x, u_y, p, \lambda)_M &= (1, 0, 0, 1, 0), \\ (\rho, u_x, u_y, p, \lambda)_R &= (3, 0, 0, 1, 1), \end{cases}$$

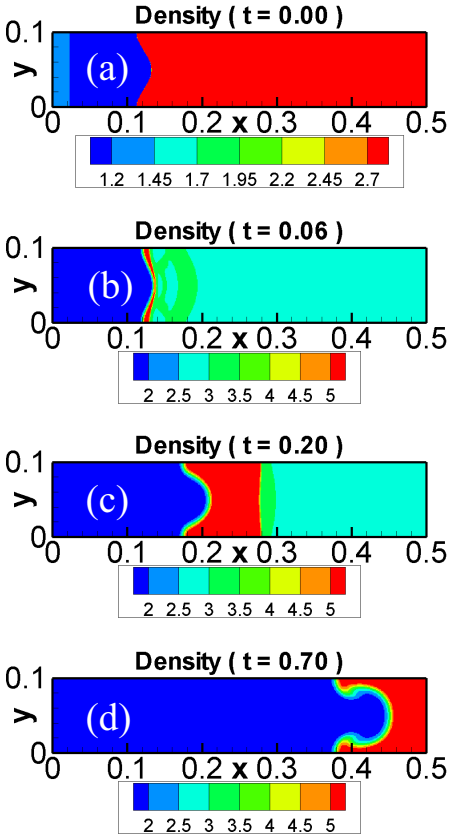

Figure 9: Snapshots of density field in the evolution of RMI at instants $t = 0.00$, 0.06, 0.20, and 0.70, respectively

where the subscripts L, M, and R indicate the regions $0 \leq x < 0.025$, $0.025 \leq x < 0.125$, and $0.125 \leq x \leq 0.5$ respectively. The initial sinusoidal perturbation, $x = 0.125 + 0.02\cos(ky)$, is applied to the physical field. The parameters $k = 20\pi$, $\theta^A = \theta^B = 2 \times 10^{-5}$, $\Delta t = 10^{-5}$, $\Delta x = \Delta y = 10^{-3}$, $N_x \times N_y = 500 \times 100$. The boundary conditions are the same as those used for KHI.

Figure 9 shows the snapshots of density field in the evolution of RMI at instants $t = 0.00$, 0.06, 0.20, and 0.70, respectively. Figure 9 (a) describes the initial density field which is divided into three parts from left to right. In Fig. 9 (b), the detonation wave passes the perturbed material interface, and the perturbation amplitude reduces quickly due to the shock compression. After that, it starts to increase and undergo the linear and nonlinear stages, see Figs.

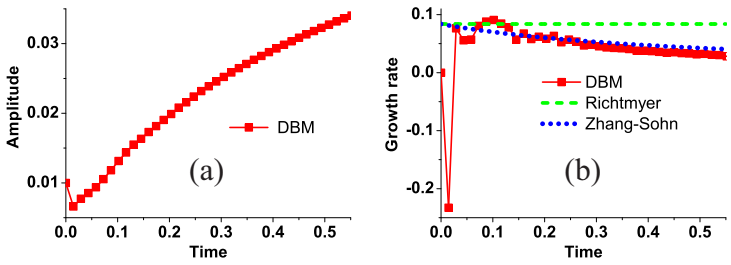

Figure 10: Amplitude (a) and growth rate (b) of the perturbed material interface in the evolution of RMI.

9 (b)-(d). And we can observe the occurrence of bubbles in the light medium and spikes in the heavy medium at time $t = 0.70$.

To have a quantitative description of the material interface, we illustrate the evolution of amplitude and growth rate, see Fig. 10. Panel (a) shows the amplitude, which is consistent with the changing density contours. Panel (b) gives the corresponding growth rate. The lines with squares denote DBM results, the dashed line denotes Richtmyer results [80] and the dotted line Zhang-Sohn results [83]. It can be found in panel (b) that the DBM results agree with both Richtmyer and Zhang-Sohn results in linear stage, and agree with Zhang-Sohn results in nonlinear stage. The reason is that Richtmyer model works only for linear stage, while Zhang-Sohn model works for linear and nonlinear stages.

4. Comparison of various DVMs

Theoretically, the more moment relations the discrete equilibrium distribution function satisfies, the more accurate the physical quantities are. However, the more discrete velocities the DVM has, the higher the computing cost is. To have a more comprehensive study on those DVMs, we need a quantitative comparison between them. It should be mentioned that this theory is independent of the value of γ. Therefore, for simplicity, we investigate D2V13 and D2V17 with $\gamma = 2$ instead of D2V16 with flexible γ. Whatever the value of γ is, the conclusion drawn from the comparison between various DVMs should be

consistent.

In this section, comparisons are made between three versions of DVM, D2V13, D2V17 and D2V33. The D2V33 model was presented by Watari and Tsutahara [67] in 2003. As same as D2V13 and D2V17, it only works for $\gamma = 2$. This model contains five groups of particle velocities: a rest particle and four groups of octagon particles with speeds ($v_a < v_b < v_c < v_d$). The moment relations satisfied by the discrete distribution function in D2V33 contain those needed to recover NS equations. To be specific, the relations in D2V33 are exactly the same as the 13 relations in D2V13 when the value of velocity $\mathbf{u}^\sigma$ is nonzero. In addition to those relations, there are other ones satisfied by the discrete distribution function in D2V33 in the case of $u_x^\sigma = 0$ and/or $u_y^\sigma = 0$. For example, it can be found that $\sum_i f_i^{\sigma eq} v_{iy}^4 = \int\int f^{\sigma eq} v_y^4 dv_x dv_y$, $\sum_i f_i^{\sigma eq} v_{ix}^3 v_{iy} = \int\int f^{\sigma eq} v_x^3 v_y dv_x dv_y$, $\sum_i f_i^{\sigma eq} v_{ix}^4 v_{iy} = \int\int f^{\sigma eq} v_x^4 v_y dv_x dv_y$, etc. in the case of $u_y^\sigma = 0$.

In the following, two sets of simulations are conducted by using the three DVMs. The first set is isothermal binary diffusion, which is a nonreactive incompressible flow. The second is steady detonation, which is a compressible system with chemical reaction. The nonequilibrium manifestations are week in the former and intense in the latter. It should be mentioned that, the DBM is based on the BGK Boltzmann equation under the condition that the moments calculated from the summation of $f_i^{\sigma eq}$ are the same with those from the integration of $f^{\sigma eq}$. From the analytical solution $\Delta_{v_x^2}^\sigma$ in Appendix B, we can find that DBM result of $\Delta_{v_x^2}^\sigma$ is at the level of the first order accuracy. Namely, with the first order accuracy, the DBM result of $\Delta_{v_x^2}^\sigma$ is consistent with that of BGK Boltzmann equation which could reflect the deviations appearing in real gases.

4.1. In the case of binary diffusion

As an example, the process of binary diffusion is simulated in six tests. Test 1 and test 2 use D2V13 with adjustable parameters (v_a, v_b, v_c, v_d, v_e) = (0.3, 1.2, 2.3, 0.2, 10^{-3}) and 1.1× (0.3, 1.2, 2.3, 0.2, 10^{-3}), respectively; Test 3 and test 4 use D2V33 with (v_a, v_b, v_c, v_d) = (0.5, 1.5, 2.5, 3.5) and 1.1× (0.5, 1.5,

2.5, 3.5), respectively; Test 5 and test 6 use D2V17 with adjustable parameters $(v_a,\, v_b,\, v_c,\, v_d,\, v_e,\, v_f) = (0.2,\, 1.2,\, 1.5,\, 1.9,\, 0.03,\, 10^{-6})$ and $1.1\times$ $(0.2,\, 1.2,\, 1.5,\, 1.9,\, 0.03,\, 10^{-6})$, respectively. Other parameters are the same as in Fig. 2.

Figure 11 shows the values of $M^A_{v_x^2}$ (a), $M^B_{v_x^2}$ (b), $\Delta^A_{v_x^2}$ (c), and $\Delta^B_{v_x^2}$ (d) in the process of binary diffusion at time $t = 0.02$. Panels (e) and (f) show the enlargements of the portions in the corresponding squares in panels (c) and (d), respectively. The simulations results by using various adjustable parameters of DVMs (test 1 − test 6) are plotted, with squares denoting test 1, diamonds denoting test 2, upper triangles denoting test 3, lower triangles denoting test 4, left triangles denoting test 5, right triangles denoting test 6. The continuous lines in panels (a) and (b) denote the analytical solution $M^\sigma_{v_x^2} = \frac{1}{2}(n^\sigma T^\sigma + \rho^\sigma u_x^{\sigma 2})$, which is obtained by substituting $f_i^\sigma = f_i^{\sigma seq}$ into Eq. (B.1). The continuous (dashed) lines in panels (c)−(f) denote Exact 1 (Exact 2) which is the analytical solution of $\Delta^\sigma_{v_x^2}$ with the first (second) order accuracy. The explicit analytic formula of $\Delta^\sigma_{v_x^2}$ is derived in Appendix B. The following points should be stressed:

(I) Figures 11 (a)−(b) show that all simulation results of $M^A_{v_x^2}$ and $M^B_{v_x^2}$ coincide with their analytical solutions. While, as shown in Figs. 11 (c)−(f), the profiles of $\Delta^A_{v_x^2}$ or $\Delta^B_{v_x^2}$ depart from each other. Mathematically, the values of $M^\sigma_{v_x^2}$ are at the level of $\mathrm{O}(\varepsilon^0)$, while those of $\Delta^\sigma_{v_x^2}$ at the level of $\mathrm{O}(\varepsilon^1)$. Therefore, the simulation results of the former (the latter) may show slight (clear) relative difference from the analytical solutions.

(II) Figures 11 (c)−(f) show that, the simulation results of $\Delta^A_{v_x^2}$ or $\Delta^B_{v_x^2}$ in test 5 and test 6 are closer to the analytical solutions than those in tests 1−4. This is because only D2V17 has all moment relations required to derive the explicit formulas of Exact 1 and Exact 2, see Appendix B. The simulation results of D2V17 are the most accurate among the three DVMs. Therefore, we use the physical quantities $(n^\sigma,\, \mathbf{u}^\sigma,\, T^\sigma)$ in test 4 to calculate the analytical solutions.

(III) It is clear in Figs. 11 (e)−(f) that test 1 and 2 have the largest relative difference and both of them are far away from the exact values; test 3 and test 4 coincide with each other and have a small departure from the exact; test 5

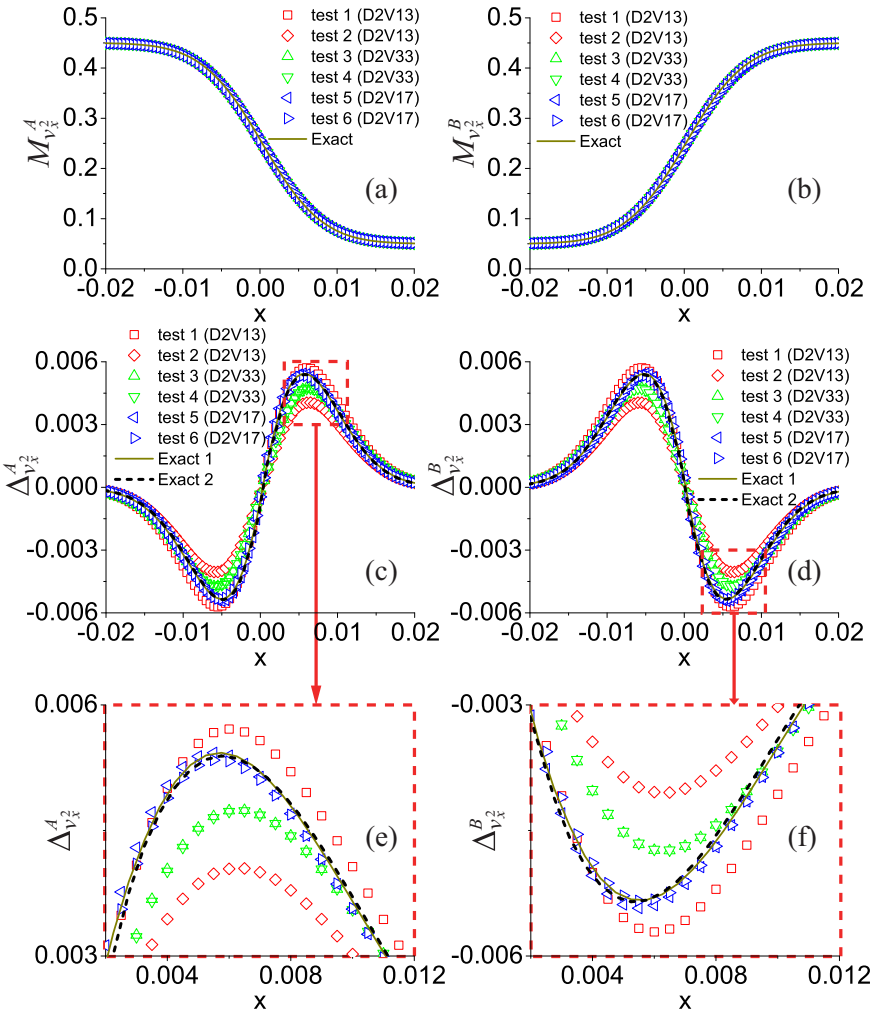

Figure 11: Profiles of $M^A_{v_x^2}$ (a), $M^B_{v_x^2}$ (b), $\Delta^A_{v_x^2}$ (c), and $\Delta^B_{v_x^2}$ (d) in the process of binary diffusion at time $t = 0.02$. Panels (e) and (f) show the enlargements of the portions in the corresponding squares in panels (c) and (d), respectively. The specific correspondences are referred to the legends.

and 6 show few relative differences and are close to the exact. The reason is that, using the DVM with more discrete velocities, the simulation results are less dependent on the adjustable parameters. Among the three DVMs, D2V13 owns the least discrete velocities and D2V33 owns the most ones.

4.2. In the case of steady detonation

To further understand the nonequilibrium manifestations simulated by the DVMs, we demonstrate them in a combustion system. The initial physical quantities read

$$\begin{cases} (\rho, u_x, u_y, p, \lambda)_L = (1.21490, 0.36515, 0, 1.75377, 1), \\ (\rho, u_x, u_y, p, \lambda)_R = (1, 0, 0, 1, 0). \end{cases}$$

The parameters are $Q = 0.2$, $T_c = 1.3$, $a_1 = 1$, $a_2 = 1$, $a_3 = 200$, $a_4 = 1$, $m^A = m^B = 1$, $\theta^A = \theta^B = 4 \times 10^{-4}$, $N_x \times N_y = 1000 \times 1$, $\Delta x = \Delta y = 10^{-3}$, $\Delta t = 10^{-4}$. The adjustable parameters are (v_a, v_b, v_c, v_d, v_e) = (0.7, 1.1, 3.9, 3.7, 10^{-3}) for D2V13, (v_a, v_b, v_c, v_d) = (1, 2, 3, 4) for D2V33, (v_a, v_b, v_c, v_d, v_e, v_f) = (3.0, 2.6, 1.1, 0.5, 3.7, 10^{-3}) for D2V17.

Figure 12 illustrates $M^A_{v_x^2}$ (a), $M^B_{v_x^2}$ (b), $\Delta^A_{v_x^2}$ (c), and $\Delta^B_{v_x^2}$ (d) in the evolution of detonation at time $t = 0.3$. We can obtain the following points.

(I) The values of $\Delta^\sigma_{v_x^2}$ are at the level of 10^{-3} in Fig. 11 and at the level of 10^{-2} in Fig. 12. Mathematically, the gradients of physical quantities (ρ^σ, u^σ_α, T^σ) are much larger in the latter than in the former. Although the nonequilibrium manifestations increase by an order of magnitude, the relative difference between Exact 1 and Exact 2 in Fig. 12 is still small. Because this difference is proportional to $\tau^{\sigma 2}$ which is a second order small quantity, Exact 1 approaches Exact 2 when τ^σ is small enough.

(II) Figure 12 shows that simulation results are close to the corresponding analytical solutions. As simple coarse-grained models, all the three DVMs can be used to investigate both hydrodynamic and thermodynamic nonequilibrium behaviors simultaneously. Although the moment relations in the DVMs are limited, the accuracy of simulation results can be raised by adjusting the adjustable

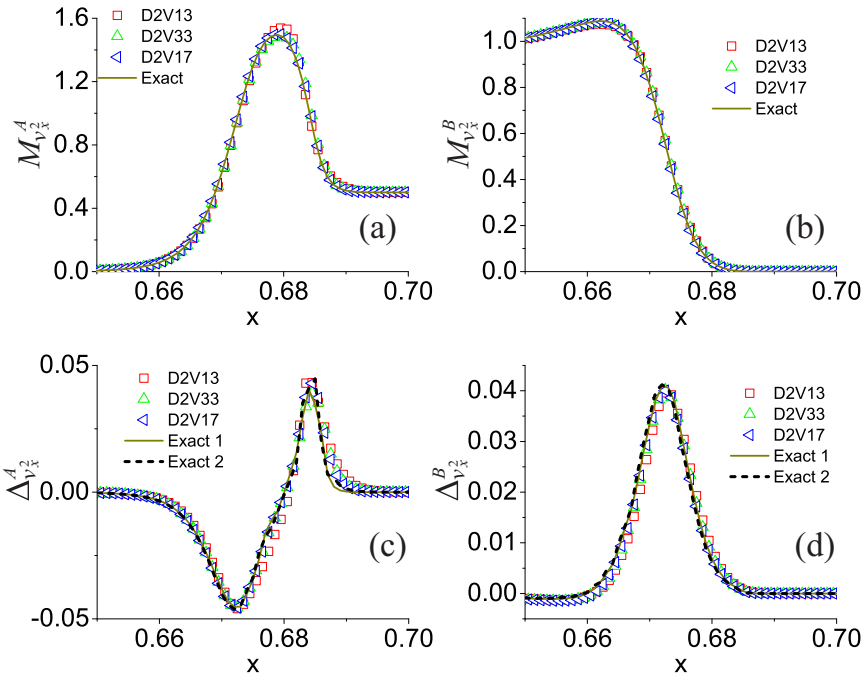

Figure 12: Profiles of $M^A_{v_x^2}$ (a), $M^B_{v_x^2}$ (b), $\Delta^A_{v_x^2}$ (c), and $\Delta^B_{v_x^2}$ (d) in the evolution of detonation at time $t = 0.3$. The specific correspondences are referred to the legends.

parameters. To obtain more accurate simulation results, we can resort to the DVM with more moment relations.

However, with discrete velocities increasing, the computational costs rise. The computing time needed for the above simulation of detonation is 7.6 s by using D2V13, 10.9 s by using D2V17, and 40.3 s by using D2V33. The computational facility used here is a personal computer with Intel(R) Core(TM) 2 CPU Q9400 @2.66GHz and RAM 4.00 GB. It is easy to find that the computing time for D2V17 is 43% more than that for D2V13, and D2V33 is about 5 times D2V13. In addition, we further simulate the same process by using D2V16 and D2V24 model [40]. The computing time is 10.6 s for D2V16 and is 19.2 s for D2V24. Obviously, the computational cost increases with increasing number of discrete velocities. Therefore, considering the contradiction between the operation efficiency and simulation precision, we should pursue a compromise strategy.

5. Conclusions

A 2-dimensional kinetic model is proposed for both subsonic and supersonic combustion phenomena. Mathematically, this model is composed of two coupled discrete Boltzmann equations for fluid behaviors and a phenomenological equation for chemical reaction process. The chemical reactant is described by one distribution function, f^A, and the product by the other distribution function, f^B. The equilibrium distribution functions, f^{Aeq} and f^{Beq}, have the same velocity and temperature.

Physically, this model is equivalent to a reactive NS model supplemented by a coarse-grained model for the thermodynamic nonequilibrium behaviours. From the kinetic model, some well-known hydrodynamic models, such as the reactive Euler and NS equations, the Fick's first and second laws, Stefan-Maxwell diffusion equation, can be easily obtained. Besides recovering hydrodynamic models, the DBM provides a simple method to measure various nonequilibrium effects. The physical accuracy of the DBM depends on the number of the ki-

netic moment relations of local equilibrium distribution function, instead of the number of discrete velocities. With increasing the moment relations, the DBM results in the nonequilibrium regimes become more reasonable. Additionally, it is straightforward to conduct a multiscale DBM simulation where the DVM is adaptively adjusted according to the local Knudsen number [40].

Acknowledgements

The authors express their great appreciation to editor Prof. Thierry J. Poinsot and the anonymous reviewers for their kind and valuable suggestions, thank Profs. Zheng Chen and Cheng Wang on helpful discussions on modeling combustion, and thank Drs. Yanbiao Gan, Huilin Lai, and Zhipeng Liu for fruitful discussions on discrete Boltzmann modeling of complex flows. AX and GZ acknowledge support of the Science Foundations of National Laboratory for Science and Technology on Computational Physics, National Natural Science Foundation of China [under Grant Nos. 11475028 and 11202003], the opening project of State Key Laboratory of Explosion Science and Technology (Beijing Institute of Technology) [under Grant No. KFJJ14-1M] and the Open Project Program of State Key Laboratory of Theoretical Physics, Institute of Theoretical Physics, Chinese Academy of Sciences, China [under Grant No. Y4KF151CJ1]. YL and CL acknowledge support of National Natural Science Foundation of China [under Grant Nos. 11574390, 41472130, and 11374360], National Basic Research Program of China [under Grant No. 2013CBA01504].

Appendix A.

D2V16

The moment relations of D2V16 are in the same form of those in Ref. [84]. The specific elements of $\hat{\mathbf{f}}^{\sigma eq}$ and $\mathbf{M}$ in D2V16 model are as follows, $\hat{f}_1^{\sigma eq} = n^\sigma$, $\hat{f}_2^{\sigma eq} = n^\sigma u_x$, $\hat{f}_3^{\sigma eq} = n^\sigma u_y$, $\hat{f}_4^{\sigma eq} = n^\sigma[(D+I)T/m^\sigma + u^2]$, $\hat{f}_5^{\sigma eq} = n^\sigma(T/m^\sigma + u_x^2)$, $\hat{f}_6^{\sigma eq} = n^\sigma u_x u_y$, $\hat{f}_7^{\sigma eq} = n^\sigma(T/m^\sigma + u_y^2)$, $\hat{f}_8^{\sigma eq} = n^\sigma u_x[(D+I+2)T/m^\sigma + u^2]$, $\hat{f}_9^{\sigma eq} = n^\sigma u_y[(D+I+2)T/m^\sigma + u^2]$, $\hat{f}_{10}^{\sigma eq} = 3n^\sigma u_x T/m^\sigma + n^\sigma u_x^3$, $\hat{f}_{11}^{\sigma eq} =$

$n^\sigma u_y T/m^\sigma + n^\sigma u_x^2 u_y$, $\hat{f}_{12}^{\sigma eq} = n^\sigma u_x T/m^\sigma + n^\sigma u_x u_y^2$, $\hat{f}_{13}^{\sigma eq} = 3n^\sigma u_y T/m^\sigma + n^\sigma u_y^3$, $\hat{f}_{14}^{\sigma eq} = n^\sigma[(D+I+2)T/m^\sigma + u^2]T/m^\sigma + n^\sigma u_x^2[(D+I+4)T/m^\sigma + u^2]$, $\hat{f}_{15}^{\sigma eq} = n^\sigma u_x u_y[(D+I+4)T/m^\sigma + u^2]$, $\hat{f}_{16}^{\sigma eq} = n^\sigma[(D+I+2)T/m^\sigma + u^2]T/m^\sigma + n^\sigma u_y^2[(D+I+4)T/m^\sigma + u^2]$; $m_{1i} = 1$, $m_{2i} = v_{ix}$, $m_{3i} = v_{iy}$, $m_{4i} = v_i^2 + \eta_i^2$, $m_{5i} = v_{ix}^2$, $m_{6i} = v_{ix}v_{iy}$, $m_{7i} = v_{iy}^2$, $m_{8i} = (v_i^2 + \eta_i^2)v_{ix}$, $m_{9i} = (v_i^2 + \eta_i^2)v_{iy}$, $m_{10i} = v_{ix}^3$, $m_{11i} = v_{ix}^2 v_{iy}$, $m_{12i} = v_{ix}v_{iy}^2$, $m_{13i} = v_{iy}^3$, $m_{14i} = (v_i^2 + \eta_i^2)v_{ix}^2$, $m_{15i} = (v_i^2 + \eta_i^2)v_{ix}v_{iy}$, $m_{16i} = (v_i^2 + \eta_i^2)v_{iy}^2$.

D2V13

Eliminating the parameters η_i and I in the relations required by D2V16 model, we get 13 linearly independent ones. The elements of $\hat{\mathbf{f}}^{\sigma eq}$ and $\mathbf{M}$ are as follows, $\hat{f}_1^{\sigma eq} = n^\sigma$, $\hat{f}_2^{\sigma eq} = n^\sigma u_x$, $\hat{f}_3^{\sigma eq} = n^\sigma u_y$, $\hat{f}_4^{\sigma eq} = n^\sigma(T/m^\sigma + u_x^2)$, $\hat{f}_5^{\sigma eq} = n^\sigma u_x u_y$, $\hat{f}_6^{\sigma eq} = n^\sigma(T/m^\sigma + u_y^2)$, $\hat{f}_7^{\sigma eq} = 3n^\sigma u_x T/m^\sigma + n^\sigma u_x^3$, $\hat{f}_8^{\sigma eq} = n^\sigma u_y T/m^\sigma + n^\sigma u_x^2 u_y$, $\hat{f}_9^{\sigma eq} = n^\sigma u_x T/m^\sigma + n^\sigma u_x u_y^2$, $\hat{f}_{10}^{\sigma eq} = 3n^\sigma u_y T/m^\sigma + n^\sigma u_y^3$, $\hat{f}_{11}^{\sigma eq} = n^\sigma[(D+2)T/m^\sigma + u^2]T/m^\sigma + n^\sigma u_x^2[(D+4)T/m^\sigma + u^2]$, $\hat{f}_{12}^{\sigma eq} = n^\sigma u_x u_y[(D+4)T/m^\sigma + u^2]$, $\hat{f}_{13}^{\sigma eq} = n^\sigma[(D+2)T/m^\sigma + u^2]T/m^\sigma + n^\sigma u_y^2[(D+4)T/m^\sigma + u^2]$; $m_{1i} = 1$, $m_{2i} = v_{ix}$, $m_{3i} = v_{iy}$, $m_{4i} = v_{ix}^2$, $m_{5i} = v_{ix}v_{iy}$, $m_{6i} = v_{iy}^2$, $m_{7i} = v_{ix}^3$, $m_{8i} = v_{ix}^2 v_{iy}$, $m_{9i} = v_{ix}v_{iy}^2$, $m_{10i} = v_{iy}^3$, $m_{11i} = v_i^2 v_{ix}^2$, $m_{12i} = v_i^2 v_{ix}v_{iy}$, $m_{13i} = v_i^2 v_{iy}^2$.

D2V17

Adding another 4 relations ($\sum_i f_i^{\sigma eq} v_{ix}^2 v_{iy}^2 = \int\int f^{\sigma eq} v_x^2 v_y^2 dv_x dv_y$, $\sum_i f_i^{\sigma eq} v_{ix} v_{iy}^3 = \int\int f^{\sigma eq} v_x v_y^3 dv_x dv_y$, $\sum_i f_i^{\sigma eq} v_{ix}^5 = \int\int f^{\sigma eq} v_x^5 dv_x dv_y$, $\sum_i f_i^{\sigma eq} v_{iy}^5 = \int\int f^{\sigma eq} v_y^5 dv_x dv_y$) to the 13 ones in D2V13, we obtain D2V17 model. The first 13 elements of $\hat{\mathbf{f}}^{\sigma eq}$ and $\mathbf{M}$ in D2V17 are the same as those in D2V13, the rest 4 ones are as follows, $\hat{f}_{14}^{\sigma eq} = n^\sigma(T/m^\sigma + u_x^2)(T/m^\sigma + u_y^2)$, $\hat{f}_{15}^{\sigma eq} = n^\sigma u_x u_y(3T/m^\sigma + u_y^2)$, $\hat{f}_{16}^{\sigma eq} = n^\sigma u_x(15T^2/m^{\sigma 2} + 10u_x^2)T/m^\sigma + u_x^4$, $\hat{f}_{17}^{\sigma eq} = n^\sigma u_y(15T^2/m^{\sigma 2} + 10u_y^2)T/m^\sigma + u_y^4$; $m_{14i} = v_{ix}^2 v_{iy}^2$, $m_{15i} = v_{ix}v_{iy}^3$, $m_{16i} = v_{ix}^5$, $m_{17i} = v_{iy}^5$.

Appendix B.

The DBM has the ability to investigate the nonequilibrium behaviors of the physical system by using the high-order moments of f_i^σ and $f_i^{\sigma eq}$ [18, 34, 35, 36,

37, 38, 39, 40]. Here we introduce

$$M^{\sigma}_{v_x^2} = \frac{1}{2}\sum_i m^{\sigma} f_i^{\sigma} v_{ix}^2, \tag{B.1}$$

$$M^{\sigma}_{v_y^2} = \frac{1}{2}\sum_i m^{\sigma} f_i^{\sigma} v_{iy}^2, \tag{B.2}$$

$$M^{\sigma}_{\eta^2} = \frac{1}{2}\sum_i m^{\sigma} f_i^{\sigma} \eta_i^2, \tag{B.3}$$

where $M^{\sigma}_{v_x^2}$, $M^{\sigma}_{v_y^2}$, $M^{\sigma}_{\eta^2}$ are the energies of species σ in the x, y and extra DOFs, respectively. Now let us introduce another three definitions

$$\Delta^{\sigma}_{v_x^2} = \frac{1}{2}\sum_i m^{\sigma}(f_i^{\sigma} - f_i^{\sigma eq}) v_{ix}^2, \tag{B.4}$$

$$\Delta^{\sigma}_{v_y^2} = \frac{1}{2}\sum_i m^{\sigma}(f_i^{\sigma} - f_i^{\sigma eq}) v_{iy}^2, \tag{B.5}$$

$$\Delta^{\sigma}_{\eta^2} = \frac{1}{2}\sum_i m^{\sigma}(f_i^{\sigma} - f_i^{\sigma eq}) \eta^2, \tag{B.6}$$

where $\Delta^{\sigma}_{v_x^2}$, $\Delta^{\sigma}_{v_y^2}$, $\Delta^{\sigma}_{\eta^2}$ denote the departures of the energies $M^{\sigma}_{v_x^2}$, $M^{\sigma}_{v_y^2}$, $M^{\sigma}_{\eta^2}$ from the equilibrium state. Additionally, other higher order moments of f_i^{σ} and $(f_i^{\sigma} - f_i^{\sigma eq})$ are referred to Refs. [18, 37, 38, 39, 40].

In fact, from the (discrete) Boltzmann equation, we can derive the relations between the nonequilibrium manifestations and physical quantities. For example, the analytical solutions $\Delta^{\sigma}_{v_\alpha^2}$ with the first and second order accuracy are given as follows. The relations between other nonequilibrium manifestations and physical quantities can be obtained in a similar way.

Equation (14) gives

$$f_i^{\sigma} - f_i^{\sigma eq} = -\tau^{\sigma}(\frac{\partial f_i^{\sigma}}{\partial t} + v_{i\alpha}\frac{\partial f_i^{\sigma}}{\partial r_\alpha} - C_i^{\sigma}). \tag{B.7}$$

Performing the operator $\frac{1}{2}\sum_i m^{\sigma} v_{i\alpha}^2$ to the two sides of Eq. (B.7) gives

$$\Delta^{\sigma}_{v_\alpha^2} = -\frac{\tau^{\sigma}}{2}\sum_i m^{\sigma}(\frac{\partial f_i^{\sigma} v_{i\alpha}^2}{\partial t} + \frac{\partial f_i^{\sigma} v_{i\alpha}^2 v_{i\beta}}{\partial r_\beta} - C_i^{\sigma} v_{i\alpha}^2). \tag{B.8}$$

Substituting the first-order truncation of distribution function, $f_i^{\sigma} \approx f_i^{\sigma seq}$, into the R.H.S of Eq. (B.8) gives

$$\Delta^{\sigma}_{v_\alpha^2} \approx \Delta^{\sigma(1)}_{v_\alpha^2}, \tag{B.9}$$

$$\Delta_{v_\alpha^2}^{\sigma(1)} = -\frac{\tau^\sigma}{2}\sum_i m^\sigma(\frac{\partial f_i^{\sigma seq} v_{i\alpha}^2}{\partial t} + \frac{\partial f_i^{\sigma seq} v_{i\alpha}^2 v_{i\beta}}{\partial r_\beta} - C_i^\sigma v_{i\alpha}^2). \tag{B.10}$$

Here the discrete equilibrium distribution function $f_i^{\sigma seq}$ depends on the macroscopic parameters of species σ, i.e., $f_i^{\sigma seq} = f_i^{\sigma seq}(n^\sigma, u^\sigma, T^\sigma)$. The temperature T^σ is defined as

$$T^\sigma = \frac{2E^{\sigma s}}{(D+I)n^\sigma}, \tag{B.11}$$

$$E^{\sigma s} = m^\sigma \sum_i \frac{1}{2} f_i^\sigma[(\mathbf{v}_i - \mathbf{u}^\sigma)^2 + \eta_i^2], \tag{B.12}$$

where $E^{\sigma s}$ is the internal energy of species σ relative to the velocity $\mathbf{u}^\sigma$ per unit volume. From Eqs. (16), (29) and (B.10), we get the first order solution

$$\begin{aligned}
\Delta_{v_\alpha^2}^{\sigma(1)} &= -\frac{\tau^\sigma}{2}[\frac{\partial}{\partial t}(n^\sigma T^\sigma + \rho^\sigma u_\alpha^{\sigma 2}) \\
&+\frac{\partial}{\partial r_\beta}(2n^\sigma T^\sigma u_\alpha^\sigma \delta_{\alpha\beta} + n^\sigma T^\sigma u_\beta^\sigma + \rho^\sigma u_\alpha^{\sigma 2} u_\beta^\sigma)] \\
&+\frac{\tau^\sigma}{2}[\rho\lambda^{\sigma\prime}(\frac{T}{m^\sigma} + u_\alpha^2) + \rho\lambda'\frac{n^\sigma}{n}(\frac{2Q}{D+I} - \frac{m^A - m^B}{m^A m^B}T)],
\end{aligned} \tag{B.13}$$

with

$$\begin{aligned}
&\frac{\partial}{\partial t}(\rho^\sigma u_\alpha^{\sigma 2}) = -2u_\alpha^\sigma \frac{\partial}{\partial r_\beta}(p^\sigma \delta_{\alpha\beta} + \rho^\sigma u_\alpha^\sigma u_\beta^\sigma) \\
&+u_\alpha^{\sigma 2}\frac{\partial}{\partial r_\beta}(\rho^\sigma u_\beta^\sigma) - 2u_\alpha^\sigma \frac{\partial}{\partial r_\beta}(P_{\alpha\beta}^\sigma + U_{\alpha\beta}^\sigma + V_{\alpha\beta}^\sigma) \\
&-2\frac{\rho^\sigma}{\tau^\sigma}u_\alpha^\sigma(u_\alpha^\sigma - u_\alpha) - \rho u_\alpha^{\sigma 2}\lambda^{\sigma\prime} + 2\rho u_\alpha u_\alpha^\sigma \lambda^{\sigma\prime},
\end{aligned} \tag{B.14}$$

$$\begin{aligned}
&\frac{\partial}{\partial t}(n^\sigma T^\sigma) = \frac{\partial}{\partial r_\alpha}[\frac{\kappa^\sigma}{m^\sigma}\frac{\partial T^\sigma}{\partial r_\alpha} + \frac{2}{D+I}(-u_\beta^\sigma P_{\alpha\beta}^\sigma + X_{\alpha\beta}^\sigma \\
&+Y_{\alpha\beta}^\sigma + Z_{\alpha\beta}^\sigma)] - \frac{\partial}{\partial r_\alpha}\rho^\sigma u_\alpha^\sigma(\frac{T^\sigma}{m^\sigma} + \frac{u^{\sigma 2}}{D+I}) + \frac{2}{D+I}p^\sigma u_\alpha^\sigma \\
&+\rho\lambda^{\sigma\prime}(\frac{T}{m^\sigma} + \frac{u^2}{D+I}) + \rho\lambda'\frac{n^\sigma}{n}(\frac{2Q}{D+I} - \frac{m^A - m^B}{m^A m^B}T) \\
&-\frac{\rho^\sigma}{\tau^\sigma}(\frac{T^\sigma - T}{m^\sigma} + \frac{u^{\sigma 2} - u^2}{D+I}) + \frac{2u_\alpha^\sigma}{D+I}\frac{\partial}{\partial r_\beta}(p^\sigma \delta_{\alpha\beta} + \rho^\sigma u_\alpha^\sigma u_\beta^\sigma) \\
&-\frac{u_\alpha^{\sigma 2}}{D+I}\frac{\partial}{\partial r_\beta}(\rho^\sigma u_\beta^\sigma) + \frac{2u_\alpha^\sigma}{D+I}\frac{\partial}{\partial r_\beta}(P_{\alpha\beta}^\sigma + U_{\alpha\beta}^\sigma + V_{\alpha\beta}^\sigma) \\
&+\frac{\rho u_\alpha^{\sigma 2}\lambda^{\sigma\prime}}{D+I} - \frac{2\rho u_\alpha u_\alpha^\sigma \lambda^{\sigma\prime}}{D+I} + \frac{2\rho^\sigma u_\alpha^\sigma}{D+I}\frac{1}{\tau^\sigma}(u_\alpha^\sigma - u_\alpha),
\end{aligned} \tag{B.15}$$

which can be obtained from Eqs. (31) − (33).

In addition, Eq. (14) gives the second-order truncation of distribution function,

$$f_i^\sigma = f_i^{\sigma seq} - \tau^\sigma (\frac{\partial f_i^{\sigma eq}}{\partial t} + v_{i\alpha}\frac{\partial f_i^{\sigma eq}}{\partial r_\alpha} + S_i^\sigma - C_i^\sigma), \tag{B.16}$$

$$S_i^\sigma = \frac{1}{\tau^\sigma}(f_i^{\sigma seq} - f_i^{\sigma eq}). \tag{B.17}$$

Substituting Eq. (B.16) into the R.S.H of Eq. (B.8) gives the second order solution,

$$\Delta_{v_\alpha^2}^\sigma \approx \Delta_{v_\alpha^2}^{\sigma(1)} + \Delta_{v_\alpha^2}^{\sigma(2)}, \tag{B.18}$$

$$\begin{aligned}\Delta_{v_\alpha^2}^{\sigma(2)} &= -\tau^\sigma \frac{\partial}{\partial t}[\Delta_{v_\alpha^2}^{\sigma(1)} - \frac{1}{2}(n^\sigma T^\sigma - n^\sigma T + \rho^\sigma u_\alpha^{\sigma 2} - \rho^\sigma u_\alpha^2)] \\ &+\frac{\tau^\sigma}{2}\frac{\partial}{\partial r_\beta}\sum_i \tau^\sigma m^\sigma (\frac{\partial f_i^{\sigma seq} v_{i\alpha}^2 v_{i\beta}}{\partial t} \\ &+\frac{\partial f_i^{\sigma seq} v_{i\alpha}^2 v_{i\beta} v_{i\chi}}{\partial r_\chi} + S_i^\sigma v_{i\alpha}^2 v_{i\beta} - C_i^\sigma v_{i\alpha}^2 v_{i\beta}).\end{aligned} \tag{B.19}$$

From Eqs. (16), (29) and (B.17), we get

$$\begin{aligned}\sum_i S_i^\sigma v_{i\alpha}^2 v_{i\beta} &= \frac{1}{\tau^\sigma}[n^\sigma (2u_\alpha^\sigma \delta_{\alpha\beta} + u_\beta^\sigma)\frac{T^\sigma}{m^\sigma} + n^\sigma u_\alpha^{\sigma 2} u_\beta^\sigma] \\ &-\frac{1}{\tau^\sigma}[n^\sigma (2u_\alpha \delta_{\alpha\beta} + u_\beta)\frac{T}{m^\sigma} + n^\sigma u_\alpha^2 u_\beta],\end{aligned} \tag{B.20}$$

$$\begin{aligned}\sum_i C_i^\sigma v_{i\alpha}^2 v_{i\beta} &= \frac{\rho\lambda'}{m^\sigma}\frac{n^\sigma}{n}(2u_\alpha \delta_{\alpha\beta} + u_\beta)(\frac{2Q}{D+I} - \frac{m^A - m^B}{m^A m^B}T) \\ &+\frac{\rho\lambda^{\sigma\prime}}{m^\sigma}(2u_\alpha \frac{T}{m^\sigma}\delta_{\alpha\beta} + u_\beta \frac{T}{m^\sigma} + u_\alpha^2 u_\beta).\end{aligned} \tag{B.21}$$

For 1-dimensional problem, Eq. (B.19) reduces to

$$\begin{aligned}\Delta_{v_\alpha^2}^{\sigma(2)} &= -\tau^\sigma \frac{\partial}{\partial t}[\Delta_{v_\alpha^2}^{\sigma(1)} - \frac{1}{2}(n^\sigma T^\sigma - n^\sigma T + \rho^\sigma u_\alpha^{\sigma 2} - \rho^\sigma u_\alpha^2)] \\ &+\frac{\tau^\sigma}{2}\frac{\partial}{\partial r_\alpha}\sum_i \tau^\sigma m^\sigma (\frac{\partial f_i^{\sigma seq} v_{i\alpha}^3}{\partial t} + \frac{\partial f_i^{\sigma seq} v_{i\alpha}^4}{\partial r_\alpha} + S_i^\sigma v_{i\alpha}^3 - C_i^\sigma v_{i\alpha}^3).\end{aligned} \tag{B.22}$$

Let us suppose that $f_i^{\sigma seq}$ satisfies the following relation,

$$\int\int f^{\sigma seq} v_\alpha^4 d\mathbf{v} d\eta = 3n^\sigma \frac{T^{\sigma 2}}{m^{\sigma 2}} + 6n^\sigma u_\alpha^{\sigma 2}\frac{T^\sigma}{m^\sigma} + n^\sigma u_\alpha^{\sigma 4} = \sum_i f_i^{\sigma seq} v_{i\alpha}^4. \tag{B.23}$$

From Eqs. (29) and (B.20) − (B.23), we get

$$\Delta_{v_\alpha^2}^{\sigma(2)} = -\tau^\sigma \frac{\partial}{\partial t}[\Delta_{v_\alpha^2}^{\sigma(1)} - \frac{1}{2}(n^\sigma T^\sigma - n^\sigma T + \rho^\sigma u_\alpha^{\sigma 2} - \rho^\sigma u_\alpha^2)]$$
$$+\frac{\tau^\sigma}{2}\frac{\partial}{\partial r_\alpha}\tau^\sigma[\frac{\partial}{\partial t}\left(3n^\sigma u_\alpha^\sigma T^\sigma + \rho^\sigma u_\alpha^{\sigma 3}\right)$$
$$+\frac{\partial}{\partial r_\alpha}(3\rho^\sigma \frac{T^{\sigma 2}}{m^{\sigma 2}} + 6n^\sigma u_\alpha^{\sigma 2} T^\sigma + \rho^\sigma u_\alpha^{\sigma 4})$$
$$+\frac{1}{\tau^\sigma}\left(3n^\sigma u_\alpha^\sigma T^\sigma + \rho^\sigma u_\alpha^{\sigma 3} - 3n^\sigma u_\alpha T - \rho^\sigma u_\alpha^3\right)$$
$$-3\rho\lambda' u_\alpha \frac{n^\sigma}{n}(\frac{2Q}{D+I} - \frac{m^A - m^B}{m^A m^B}T) - \rho\lambda^{\sigma\prime}(3u_\alpha \frac{T}{m^\sigma} + u_\alpha^3)]. \quad \text{(B.24)}$$

Mathematically, $\Delta_{v_\alpha^2}^{\sigma(1)}$ is proportional to τ^σ at the level of $\mathrm{O}(\varepsilon^1)$, and $\Delta_{v_\alpha^2}^{\sigma(2)}$ is proportional to $\tau^{\sigma 2}$ at the level of $\mathrm{O}(\varepsilon^2)$.

It should be pointed that the moment relation in Eq. (B.23) is satisfied by the discrete distribution function in D2V17, but not in D2V13 or D2V33. Performing the operator $\sum_i m^\sigma v_{i\alpha}^4$ to the expression of $f_i^{\sigma seq}$ in D2V33 [67] gives

$$\sum_i f_i^{\sigma seq} v_{i\alpha}^4 = 3n^\sigma \frac{T^{\sigma 2}}{m^{\sigma 2}} + 6n^\sigma u_\alpha^{\sigma 2}\frac{T^\sigma}{m^\sigma} + \frac{9}{8}n^\sigma u_\alpha^{\sigma 4}. \quad \text{(B.25)}$$

The difference between the above equation and Eq. (B.23) is $\frac{1}{8}n^\sigma u_\alpha^{\sigma 4}$. If u_α^σ is small enough, the difference is negligible, otherwise not negligible.

Note that the more moment relations the DVM has, the more accurate the nonequilibrium manifestations are. One can simply increase the physical accuracy of the DBM in describing TNE via using more kinetic moment relations. A further discussion is beyond this work.

References

[1] S. Chu and A. Majumdar, Opportunities and challenges for a sustainable energy future, Nature (London), 488 (2012) 294-303.

[2] K. K. Kuo, *Principles of combustion*, John Willey & Sons, New York 1986.

[3] C. K. Law, *Combustion physics*, Cambridge University Press, Cambridge 2006.

[4] W. Fickett and W. C. Davis, *Detonation: Theory and Experiment*, Dover, New York 2000.

[5] J. H. S. Lee, *The detonation phenomenon*, Cambridge University Press, Cambridge 2008.

[6] B. Lewis and G. V. Elbe, *Combustion, flames and explosions of gases*, Academic Press Inc., London 1987.

[7] E. S. Oran and J. P. Boris, *Numerical simulation of reactive flow*, Cambridge University Press, New York 2005.

[8] Y. Ju, Recent progress and challenges in fundamental combustion research, Adv. Mech. 44 (2014) 1-72.

[9] E. Nagnibeda and E. Kustova, *Non-Equilibrium Reacting Gas Flows*, Springer, Berlin 2009.

[10] S. Succi, *The Lattice Boltzmann Equation for Fluid Dynamics and Beyond*, Oxford University Press, New York, 2001.

[11] R. Benzi, M. Sbragaglia, M. Bernaschi, and S. Succi, Phase-field model of long-time glasslike relaxation in binary fluid mixtures, Phys. Rev. Lett. 106 (2011) 164501.

[12] Michael R. Swift, E. Orlandini, W. R. Osborn, and J. M. Yeomans, Lattice Boltzmann simulations of liquid-gas and binary fluid systems, Phys. Rev. E. 54 (1996) 5041-5052.

[13] A. J. Wagner and J. M. Yeomans, Breakdown of scale invariance in the coarsening of phase-separating binary fluids, Phys. Rev. Lett. 80 (1998) 1429-1432.

[14] R. J. Vrancken, M. L. Blow, H. Kusumaatmaja, K. Hermans, A. M. Prenen, C. W. M. Bastiaansen, D. J. Broer, and J. M. Yeomans, Anisotropic wetting and de-wetting of drops on substrates patterned with polygonal posts, Soft Matter 9 (2013) 674-683.

[15] R. Ledesma-Aguilar, D. Vella, and J. M. Yeomans, Lattice-Boltzmann simulations of droplet evaporation, Soft Matter 10 (2014) 8267-8275.

[16] Y. Liu, L. Moevius, X. Xu, T. Qian, J. M. Yeomans and Z. Wang, Pancake bouncing on superhydrophobic surfaces, Nat. Phys. 10 (2014) 515-519.

[17] M. A. Mazloomi, S. S. Chikatamarla, and I. V. Karlin, Entropic Lattice Boltzmann Method for Multiphase Flows, Phys. Rev. Lett. 114 (2015) 174502.

[18] Y. Gan, A. Xu, G. Zhang, and S. Succi, Discrete Boltzmann modeling of multiphase flows: hydrodynamic and thermodynamic non-equilibrium effects, Soft Matter 11 (2015) 5336C5345.

[19] S. Succi, G. Bella, and F. Papetti, Lattice kinetic theory for numerical combustion, J. Sci. Comput. 12 (1997) 395-408.

[20] O. Filippova and D. Hänel, Lattice-BGK Model for Low Mach Number Combustion, Int. J. Mod. Phys. C 9 (1998) 1439-1445.

[21] O. Filippova and D. Hänel, A novel lattice bgk approach for low mach number combustion, J. Comput. Phys. 158 (2000) 139-160.

[22] O. Filippova and D. Hänel, A novel numerical scheme for reactive flows at low Mach numbers, Comput. Phys. Commun. 129 (2000) 267-274.

[23] H. Yu, L. S. Luo, and S. S. Girimaji, Scalar mixing and chemical reaction simulations using lattice Boltzmann method, Int. J. Comput. Eng. Sci. 3 (2002) 73-87.

[24] K. Yamamoto, X. He, and G. D. Doolen, Simulation of combustion field with lattice boltzmann method, J. Stat. Phys. 107 (2002) 367-383.

[25] K. Yamamoto, LB simulation on combustion with turbulence, Int. J. Mod. Phys. B 17 (2003) 197-200.

[26] K. Yamamoto, N. Takada, and M. Misawa, Combustion simulation with Lattice Boltzmann method in a three-dimensional porous structure, Proc. Comb. Inst. 30 (2005) 1509-1515.

[27] T. Lee, C. Lin, and L. D. Chen, A lattice boltzmann algorithm for calculation of the laminar jet diffusion flame, J. Comput. Phys. 215 (2006) 133-152.

[28] E. Chiavazzo, I. V. Karlin, A. N. Gorban and K. Boulouchos, Combustion simulation via lattice Boltzmann and reduced chemical kinetics, J. Stat. Mech: Theory Exp. 2009 (2009) P06013.

[29] E. Chiavazzo, I. V. Karlin, A. N. Gorban, and K. Boulouchos, Coupling of the model reduction technique with the lattice Boltzmann method for combustion simulations, Combust. Flame 157 (2010) 1833-1849.

[30] E. Chiavazzo, I. V. Karlin, A. N. Gorban, and K. Boulouchos, Efficient simulations of detailed combustion fields via the lattice Boltzmann method, Int. J. Numer. Methods Heat Fluid Flow 21 (2011) 494-517.

[31] S. Chen and C. Zheng, Counterflow diffusion flame of hydrogen-enriched biogas under MILD oxy-fuel condition, Int. J. Hydrogen Energ. 36 (2011) 15403-15413.

[32] S. Chen, J. Mi, H. Liu, and C. Zheng, First and second thermodynamic-law analyses of hydrogen-air counter-flow diffusion combustion in various combustion modes, Int. J. of Hydrogen Energ. 37 (2012) 5234-5245.

[33] M. L. Rocca, A. Montessori, P. Prestininzi, and S. Succi, A multispeed Discrete Boltzmann Model for transcritical 2D shallow water flows, J. Comput Phys. 284 (2015) 117-132.

[34] A. Xu, G. Zhang, Y. Gan, F. Chen, and X. Yu, Lattice Boltzmann modeling and simulation of compressible flows, Front. Phys. 7 (2012) 582-600.

[35] A. Xu, G. Zhang, Y. Li, and H. Li, Modeling and Simulation of Nonequilibrium and Multiphase Complex Systems: Lattice Boltzmann kinetic Theory and Application (in Chinese), Prog. Phys. 34 (2014) 136-167.

[36] A. Xu, G. Zhang, Y. J. Ying, Progress of discrete boltzmann modeling and simulation of combustion system (in chinese), Acta. Phys. Sin. 64 (2015) 184701.

[37] B. Yan, A. Xu, G. Zhang, Y. Ying, and H. Li, Lattice Boltzmann model for combustion and detonation, Front. Phys. 8 (2013) 94-110.

[38] C. Lin, A. Xu, G. Zhang, Y. Li, S. Succi, Polar-coordinate lattice Boltzmann modeling of compressible flows, Phys. Rev. E 89 (2014) 013307.

[39] C. Lin, A. Xu, G. Zhang, Y. Li, Polar Coordinate Lattice Boltzmann Kinetic Modeling of Detonation Phenomena, Commun. Theor. Phys. 62 (2014) 737-748.

[40] A. Xu, C. Lin, G. Zhang and Y. Li, Multiple-relaxation-time lattice Boltzmann kinetic model for combustion, Phys. Rev. E 91 (2015) 043306.

[41] R. Benzi, R. Tripiccione, F. Massaioli, S. Succi, S. Ciliberto, On the scaling of the velocity and temperature structure functions in rayleigh-bénard convection, Europhys. Lett. 25 (1994) 341C346.

[42] V. Novozhilov and C. Byrne, Lattice Boltzmann modeling of thermal explosion in dynamic mixtures, AIP Conf. Proc. 1479 (2012) 82-85.

[43] Y. Gan, A. Xu, G. Zhang, and Y. Li, Lattice Boltzmann study on Kelvin-Helmholtz instability: Roles of velocity and density gradients, Phys. Rev. E 83 (2011) 056704.

[44] F. Chen, A. Xu, G. Zhang, Y. Li and S. Succi, Multiple-relaxation-time lattice Boltzmann approach to compressible flows with flexible specific-heat ratio and Prandtl number, Europhys. Lett. 90 (2010) 54003.

[45] X. Shan and H. Chen, Lattice Boltzmann model for simulating flows with multiple phases and components, Phys. Rev. E 47 (1993) 1815-1820.

[46] X. Shan and G. Doolen, Diffusion in a multicomponent lattice Boltzmann equation model, Phys. Rev. E 54 (1996) 3614-3620.

[47] X. Shan, Multicomponent lattice Boltzmann model from continuum kinetic theory, Phys. Rev. E 81 (2010) 045701.

[48] N. S. Martys and H. Chen, Simulation of multicomponent fluids in complex three-dimensional geometries by the lattice Boltzmann method, Phys. Rev. E 53 (1996) 743.

[49] V. Sofonea and R. F. Sekerka, BGK models for diffusion in isothermal binary fluid systems, Physica A 299 (2001) 494-520.

[50] L. S. Luo and S. S. Girimaji, Lattice Boltzmann model for binary mixtures, Phys. Rev. E 66 (2002) 035301.

[51] L. S. Luo and S. S. Girimaji, Theory of the lattice Boltzmann method: Two-fluid model for binary mixtures, Phys. Rev. E 67 (2003) 036302.

[52] A. Xu, Finite-difference lattice-Boltzmann methods for binary fluids, Phys. Rev. E 71 (2005) 066706.

[53] A. Xu, Two-dimensional finite-difference lattice Boltzmann method for the complete Navier-Stokes equations of binary fluids, Europhys. Lett. 69 (2005) 214-220.

[54] M. E. McCracken and J. Abraham, Lattice Boltzmann methods for binary mixtures with different molecular weights, Phys. Rev. E 71 (2005) 046704.

[55] S. Arcidiacono, S. Ansumali, I. V. Karlin, J. Mantzaras, and K. B. Boulouchos, Entropic lattice Boltzmann method for simulation of binary mixtures, Math. Comput. Simul. 72 (2006) 79-83.

[56] S. Arcidiacono, J. Mantzaras, S. Ansumali, I. V. Karlin, C. Frouzakis, and K. B. Boulouchos, Simulation of binary mixtures with the lattice Boltzman method, Phys. Rev. E 74, 056707 (2006).

[57] S. Arcidiacono, I. V. Karlin, J. Mantzaras, and C. E. Frouzakis, Lattice Boltzmann model for the simulation of multicomponent mixtures, Phys. Rev. E 76 (2007) 046703.

[58] P. Asinari, Multiple-relaxation-time lattice Boltzmann scheme for homogeneous mixture flows with external force, Phys. Rev. E 77 (2008) 056706.

[59] P. Asinari, Lattice Boltzmann scheme for mixture modeling: Analysis of the continuum diffusion regimes recovering Maxwell-Stefan model and incompressible Navier-Stokes equations, Phys. Rev. E 80 (2009) 056701.

[60] Q. Li and A. J. Wagner, Symmetric free-energy-based multicomponent lattice Boltzmann method, Phys. Rev. E 76 (2007) 036701.

[61] R. Benzi, M. Sbragaglia, S. Succi, M. Bernaschi, and S. Chibbaro, Mesoscopic lattice Boltzmann modeling of soft-glassy systems: Theory and simulations, J. Chem. Phys. 131 (2009) 104903.

[62] J. Kang, N. I. Prasianakis, and J. Mantzaras, Lattice Boltzmann model for thermal binary-mixture gas flows, Phys. Rev. E 87 (2013) 053304.

[63] J. Kang, N. I. Prasianakis, and J. Mantzaras, Thermal multicomponent lattice Boltzmann model for catalytic reactive flows, Phys. Rev. E 89 (2014) 063310.

[64] M. Watari, Finite difference lattice Boltzmann method with arbitrary specific heat ratio applicable to supersonic flow simulations, Physica A 382 (2007) 502-522.

[65] S. G. Cochran and J. Chan, Shock Initiation and Detonation in One and Two Dimensions, Lawrence Livermore National Laboratory Report No. UCID-18024, 1979 (unpublished).

[66] H. Zhang and F. Zhuang, NND Schemes and Their Applications to Numerical Simulation of Two- and Three-Dimensional Flows, Adv. Appl. Mech. 29 (1991) 193-256.

[67] M. Watari and M. Tsutahara, Two-dimensional thermal model of the finite-difference lattice boltzmann method with high spatial isotropy, Phys. Rev. E 67 (2003) 036306.

[68] M. E. Glicksman, Diffusion in Solids: Field Theory, Solid-State Principles and Applications, John Wiley & Sons, Inc., New York, 2000.

[69] F. Williams, *Combustion Theory*, Benjamin/Cumming, California, 1985.

[70] F. C. Lockwood, The modelling of turbulent 855 premixed and diffusion combustion in the computation of engineering flows, Combust. Flame 29 (1977) 111-122.

[71] A. M. Khokhlov, E. S. Oran, A. Y. Chtchelkanova, J. C. Wheelerc, Interaction of a shock with a sinusoidally perturbed flame, Combust. Flame 117 (1999) 99-116.

[72] Ya. B. Zeldovich, On the theory of the propagation of detonation in gaseous systems, J. Exp. Theor. Phys., 10 (1940) 542-568.

[73] J. Von Neumann, *Theory of Detonation Waves*, New York: Macmillan, 1942.

[74] W. Döering, On detonation processes in gases, Ann. Phys., 43 (1943) 421-436.

[75] D. L. Chapman, On the rate of explosion in gases, Philos. Mag, 47 (1899) 90-104.

[76] E. J. Jouguet, On the propagation of chemical reactions in gases, J. Math. Pures Appl, 1 (1905) 347-425.

[77] S. Chandrasekhar, *Hydrodynamic and Hydromagnetic Stability*, Oxford University Press, London, 1968.

[78] M. F*ü*ri, P. Papas, R. M. Raïs, P. A. Monkewitz, The effect of flame position on the kelvin-helmholtz instability in non-premixed jet flames, Proc. Combus. Inst. 29 (2002) 1653-1661.

[79] L. Wang, W. Ye, Y. Li, Combined effect of the density and velocity gradients in the combination of Kelvin-Helmholtz and Rayleigh-Taylor instabilities, Phys. Plasmas, 17 (2010) 042103.

[80] R. D. Richtmyer, Taylor instability in shock acceleration of compressible fluids, Comm. Pure Appl. Math. 13 (1960) 297-319.

[81] E. E. Meshkov, Instability of the interface of two gases accelerated by a shock wave, Fluid Dyn. 4 (1969) 101-104.

[82] A. M. Khokhlov, E. S. Oran, G. O. Thomas, Numerical simulation of deflagration-to-detonation transition: the role of shock-flame interactions in turbulent flames, Combust. Flame 117 (1999) 323-339.

[83] Q. Zhang and S. I. Sohn, Padé approximation to an interfacial fluid mixing problem, Appl. Math. Lett. 10 (1997) 121-127.

[84] Y. Gan, A. Xu, G. Zhang, and Y. Yang, Lattice BGK kinetic model for high-speed compressible flows: Hydrodynamic and nonequilibrium behaviors, Europhys. Lett. 103 (2013) 24003.